

Full Length Article

Development of carbon sphere/ceria (CS/CeO₂) heterostructured particles and their applications to functional abrasives toward photochemical mechanical polishing

Tianyu Wang ^a, Yue Chen ^b, Ailian Chen ^{a,*}, Yang Chen ^{b,*}^a School of Mechanical Engineering, Changzhou University, Changzhou, Jiangsu 213164, PR China^b School of Materials Science and Engineering, Changzhou University, Changzhou, Jiangsu 213164, PR China

ARTICLE INFO

ABSTRACT

Keywords:

Carbon/ceria hybrids
Functional abrasives
Cooperative effect
Removal mechanism
Photochemical mechanical polishing (PCMP)

Ceria (CeO₂) possesses tribochemical ability and photochemical oxidation activity simultaneously. Herein, novel carbon-coupled CeO₂ heterostructures were developed as functional abrasives toward photochemical mechanical polishing (PCMP) system. Polydispersed carbon spheres (CS) were uniformly grafted with pure and Y-doped CeO₂ nanocrystals via an *in-situ* chemical precipitation approach. The resulting CS/CeO₂ and CS/CeYO₂ core/shell hybrids were characterized by X-ray diffraction, scanning electron microscopy, transmission electron microscopy, Fourier transform infrared spectroscopy, X-ray photoelectron spectroscopy, photoluminescence spectroscopy, and Raman spectroscopy. As confirmed by atomic force microscope, the developed hybrid abrasives allowed the nearly non-damage surfaces with angstrom-level roughness (0.10–0.13 nm Ra, 0.14–0.16 nm RMS, within 5.0 × 5.0 μm²) in both CMP and PCMP experiments over oxide films. As expected, introduction of ultraviolet radiation and/or Y-doping modification were effective in enhancing removal rates (RR). The CS/CeYO₂ abrasives offered a ca. 196% increment of RR-PCMP compared to the RR-CMP of undoped ones (139 nm/min vs 47 nm/min). The improved PCMP performance might be attributed to the cooperative effects of the CS/CeO₂ heterostructures (overall modulus reduction, CS-CeO₂ heterojunction construction, surface defect manipulation, etc.). The possible PCMP mechanism over CS/CeO₂ was also discussed on the basis of the interfacial contact, the photochemical modification, and the tribochemical removal.

1. Introduction

Chemical mechanical polishing (or planarization, CMP) [1–3] is a process that removes materials by the synergy of chemical and mechanical actions to achieve highly planarized surfaces with angstrom-level roughness. As one of important components in CMP systems, metal oxide nanoparticles (NPs) such as silica (SiO₂), ceria (CeO₂), alumina (Al₂O₃), etc. are the most popular inorganic abrasives in polishing slurries. Colloidal SiO₂ slurry is commonly used for CMP process steps in integrated circuit manufacturing such as monocrystalline silicon, shallow trench isolation, tungsten, copper, copper barrier metal (e.g., TaN/Ta), etc. SiO₂ NPs are also widely applied to develop novel green CMP slurries toward sapphire, diamond, titanium, copper, nickel, etc. [1–6] for achieving high-quality surfaces in semiconductor, microelectronics, optoelectronics, and aerospace industries. In-depth investigations on macroscale friction and wear of particles are essential to

develop CMP slurries for next-generation devices including new materials and complex structures. As reported by Zhang and coworkers [7], macroscale superlubricity on macroscale surfaces was firstly realized under ambient conditions, which was performed on the graphene coated silica surfaces.

CeO₂ NPs have been extensively investigated in multiple applications due to their excellent physiochemical, photocatalytic, electrical, and mechanical characteristics, as well as unique valence transition properties [8–10]. As one of the most popular abrasives in CMP applications, CeO₂ NPs [11–16] and CeO₂-based composites [17–25] have been introduced into the ultra-precision manufacturing of integrated circuits (typically dielectric films), ceramics, optical systems, microelectromechanical systems, etc.

In CeO₂ lattices, there are coexistence of Ce³⁺ and Ce⁴⁺ oxidation states and presence of intrinsic oxygen vacancies (Vo). It has been proposed that Ce³⁺ ions, instead of Ce⁴⁺ species at CeO₂ abrasive surfaces,

* Corresponding authors.

E-mail addresses: cy_cczu@126.com (A. Chen), cy_jpu@126.com (Y. Chen).

provide the assistance to the breaking up of Si–O bond during dielectric CMP, thus allowing a high removal efficiency over silica materials. For example, Kim and coworkers [11] reported a facile strategy to synthesize CeO₂ NPs with tunable Ce³⁺ concentrations. It was also verified that an increased Ce³⁺ content contributed to an enhanced chemisorption between CeO₂ abrasives and silicate anions during oxide-CMP, which might be responsible for the improved removal rate toward SiO₂ films. Additionally, Cheng and coworkers [13] synthesized lanthanide metals (La, Nd and Yb) doped CeO₂ NPs through a modified incipient impregnation method for Ce³⁺ content enrichments. As revealed by XPS experiments and density function theory calculation, the introduction of trivalent lanthanide species contributed to the Vo formation energy reductions, thus facilitating the formation of Vo and transition from Ce⁴⁺ to Ce³⁺ in CeO₂. CMP experiments showed that both polishing rate and surface quality of silica wafer were obviously improved using the doped CeO₂ NPs. Kelvin probe force microscopy investigations [16] further revealed that the formation of V_O and the reduction of Ce⁴⁺ to Ce³⁺ contributed to increasing the electron density and Fermi level of the CeO₂ NPs after doping with trivalent lanthanides.

As one of typical N-type semiconductors, CeO₂ NPs have been widely applied in photocatalytic/photochemical oxidation processes due to their abundant surface defects (typically Vo and Ce³⁺), admirable redox ability, and low-cost effectiveness [26,27]. Nevertheless, wide bandgap (typically 2.8–3.2 eV), unsatisfactory light absorption, easy recombination of photoexcited charges highly restrict the practical applications and photooxidation activity improvements of CeO₂ systems. Coupling with other materials and/or introduction of dopants [28–32] are the effective approaches to overcome the disadvantages. For example, combination of CeO₂ NPs and carbon materials (typically graphene, nanotubes, fullerenes, carbon quantum dots, etc.) [30–32] is gaining great attention nowadays for improved photochemical/phocatalytic oxidation activities. For carbon-coupled CeO₂ systems, the carbon skeleton can provide additional charge transfer pathways. Consequently, the heterogeneous structures can effectively prolong the lifetime of photon-generated charges, which contributes to the enhancement of photooxidation activities.

A typical CMP process commonly involves the dynamic synergy of chemical surface modification and mechanical (or tribochemical) material removal. Up to now, a series of surface treatment techniques such as photochemical/phocatalytic oxidation [33–35], electrochemical oxidation [36,37], Fenton oxidation [34,38], ozone oxidation [39], laser oxidation [40], etc. have been introduced into conventional CMP for enhancing chemically reacted activity and thus improving material removal efficiency. Among these methods, photooxidation technique offers several advantages, such as easy operation, high efficiency, less energy consumption, minimal secondary pollution, etc. Up to now, the mixed NPs (typically involved SiO₂ and TiO₂) [33–35] are the most commonly used abrasive systems in photochemical/phocatalytic oxidation-assisted mechanical polishing (PCMP) applications. These are few reports focused on the design and usage of CeO₂-based composites as functional abrasives in PCMP systems, excepting polystyrene/ceria-titania [41], polystyrene/ceria [42], meso-silica/Er-doped ceria [43], and polystyrene/polyaniline/ceria [44]. Nevertheless, these composites as novel abrasives have some drawbacks such as high cost and complicated synthesis, which highly restrict their practical and commercial applications. There has grown up an urgent need for the simple and effective fabrications of high-performance abrasives over PCMP systems.

In order to resolve these bottleneck problems, it is highly essential to develop the functional abrasives featuring both high photochemical/phocatalytic and mechanical/tribochemical activities toward improved PCMP performances. Significantly, CeO₂ materials possess photooxidation modification activity and tribochemical removal ability simultaneously, which may be ideal for the development of the functional abrasive systems toward PCMP.

Inspired by the previous works, herein we report some of our recent

research activities in novel functional hybrid abrasives. In this work, pure and Y-doped CeO₂ nanocrystals were uniformly grafted on the surfaces of carbon spheres (CS) synthesized via a simple and facile glucose hydrothermal approach. The physicochemical properties of the resulting CS/CeO₂ hybrids were systematically examined via powder X-ray diffraction, field emission scanning electron microscopy, high resolution transmission electron microscopy, Fourier transform infrared spectroscopy, X-ray photoelectron spectroscopy, photoluminescence spectroscopy, and Raman spectroscopy techniques. The aim of Y-doping in CeO₂ is to generate more surface defects (typically Vo and Ce³⁺), thus allowing tribochemical and photochemical activity improvements for enhanced removal efficiency. The purpose of CS is to form a heterojunction with CeO₂ for synergistically inhibited recombination of photoinduced pairs, thereby leading to the further enhancement of photooxidation activity. Herein, the CeO₂ shells and the CS cores can serve as an electron donor and an electron acceptor, respectively. Meanwhile, the low-modulus CS is also expected to reduce the overall modulus of the proposed hybrids for improved surface quality. The CMP and PCMP performances of the heterostructured abrasives were evaluated in terms of surface morphology and roughness, topographical variation, as well as removal efficiency. It was confirmed that the as-proposed functional CS/CeO₂ abrasives allowed the formations of ultra-precise and nearly non-damage surfaces with angstrom-level roughness under both CMP and PCMP conditions. As expected, introduction of ultraviolet radiation and/or Y-doping modification were effective in enhancing material removal efficiency of CS/CeO₂ abrasives. The improved polishing performances might be attributed to the physicochemical characteristics of the CS/CeO₂ heterostructures, such as overall modulus reduction, CS–CeO₂ heterojunction construction, surface defect (Vo and Ce³⁺) manipulation, etc. This work aims to provide a novel approach to developing functional abrasive systems that can improve both surface quality and removal rate. To the best of our knowledge, this is the first report about the Cs-coupled CeO₂ heterostructures as novel functional abrasives for improved PCMP performance.

2. Experimental section

2.1. Materials

D(+)–Glucose monohydrate (C₆H₁₂O₆·H₂O), hexamethylenetetramine (HMT), sodium hydroxide (NaOH), ethanol absolute, acetone, cerium nitrate hexahydrate (Ce(NO₃)₃·6H₂O), yttrium nitrate hexahydrate (Y(NO₃)₃·6H₂O), and hydrogen peroxide (supplied as 30% aqueous solution) were obtained from Shanghai Chemical Reagent Co., Ltd. (China). Deionized (DI) water was used throughout the experiments. All chemicals were of analytical grade and used as received without further purification.

2.2. Synthesis of heterostructured particles

Polydispersed CS with multiple particle sizes were fabricated via a one-pot hydrothermal approach [45] in the presence of Glucose as a carbon source. In a typical synthesis, glucose (10 g) was charged into 50 g of DI water in a Teflon-lined autoclave (100 mL). After complete dissolution of glucose, the autoclave was placed into a pre-heated oven and maintained at temperatures of 180 °C for time up to 4 h, and then cooled to room temperature. To ensure the carbonization of glucose and the formation of amorphous carbon, the proposed hydrothermal temperature is slightly higher than that of the normal glycosidation temperature of glucose. In this work, the resulting black or dark grey suspensions containing CS particles were directly utilized in subsequent preparations of pure and Y-doped CS/CeO₂ hybrids.

In the fabrication of CS/CeYO₂ hybrids, the as-prepared CS suspension (40 g) were dispersed in DI water (80 g) with ultrasonic vibration for 10 min, followed by the addition of 0.72 g of Ce(NO₃)₃·6H₂O, 0.07 g

of $\text{Y}(\text{NO}_3)_3 \cdot 6\text{H}_2\text{O}$, and 1.28 g of HMT (dissolved in 40 g of DI water). Herein, the molar ratio of Y/(Ce + Y) in the Y-doped CeO_2 solid solution was set to 0.1. Subsequently, the above mixture was slowly heated to 75 °C in a water bath, and the reaction was performed under magnetic stirring (300 rpm) for 2 h at 75 °C. The resulting products were purified by repeated centrifugation and washed with DI water and ethanol several times, followed by drying at 80 °C and calcined at 550 °C in a nitrogen atmosphere for 2 h.

For comparison, the undoped CS/ CeO_2 composites were also prepared using a similar procedure described above with little modifications. Identical conditions as the previous syntheses were used, except that $\text{Ce}(\text{NO}_3)_3 \cdot 6\text{H}_2\text{O}$ (0.8 g) were introduced into the CS/ CeO_2 preparation.

2.3. Characterization and measurements

The phase structures of the products were analyzed using a powder X-ray diffractometer (XRD, D/Max 2500 PC, Rigaku) with Cu-K α radiation ($\lambda = 1.4518 \text{ \AA}$) over the 2θ ranging from 20° to 80°. Compositional investigations were carried out with Fourier transform infrared spectroscopy (FT-IR, Avatar 370, Nicolet). Field-emission scanning electron microscopy (FESEM) observations were performed on a SUPRA-55 microscope (ZEISS) at an accelerating voltage of 5 kV. Transmission electron microscopy (TEM) and high-resolution TEM (HRTEM) images were obtained on an electron microscope (JEM-2100, JEOL) operating at an accelerating voltage of 120 kV. Photoluminescence (PL) spectra were recorded on a PerkinElmer LS45 fluorescence spectrometer (PL). X-ray photoelectron spectroscopy (XPS) spectra were obtained using a Ulvac-Phi PHI-5000 VP III spectrometer with Al K α radiation ($h\nu = 1486.6 \text{ eV}$). The particle-size distribution based on the dynamic light scattering (DLS) method was performed on a Zetasizer Nano ZS apparatus (Malvern Instruments, UK) using a He-Ne laser (633 nm) with a scattering angle of 173°.

2.4. CMP and PCMP experiments

Fig. 1 presents the schematic view of the CMP/PCMP experimental set-up. In the CMP experiments, a rotary-type polishing machine (TegraForce-1/TrgraPol-15, Struers, Denmark) coupled with a porous polyurethane pad (MD-Chem, Struers) were utilized to finish the silicon oxide wafers (ca. 1200 nm in oxide layer thickness). In the case PCMP, a commercially available halogen lamp (250 W) with a wavelength of 365 nm was used as an UV-light source. The photon energy of the UV-light should be higher than the band-gap energy of CeO_2 photocatalysts in order to ensure the excitation of photon-generated carriers at CeO_2 surfaces. In our experimental conditions, the applied UV-light source with 365 nm of wavelength can provide a photon energy of ca. 3.4 eV, which is higher than the energy gap of CeO_2 (typically 3.0 eV). Every polishing test was conducted at 3.6 psi down pressure for 2 min. The

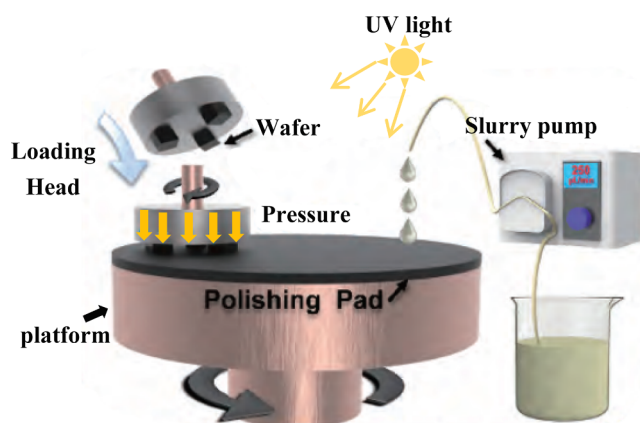


Fig. 1. Schematic view of the polishing experimental set-up.

rotation speeds of the head and platen were 120 and 90 rpm, respectively. And the flow rate of polishing slurry (1 wt% in solid content) was fixed at 50 mL/min. For slurry preparations, the particle abrasives (1 g) were dispersed in DI water (100 g) under ultrasonic condition. And the pH values of the polishing slurries were adjusted to near 8.0 by 0.1 M NaOH solution. Prior to PCMP, the prepared slurries were irradiated by an UV lamp under ultrasonic treatment for 10 min. After CMP and PCMP experiments, the wafers were repeatedly cleaned by sonication in acetone and DI water, and dried by nitrogen flow before morphology investigations.

The high-resolution surface morphologies of the wafers before and after polishing were determined by an atomic force microscope (AFM, Nanoman VS, Bruker, equipped with a Dimension V controller) in tapping mode. Commercially available AFM probes (Tap300Al-G, Budget-Sensors) with a tip radius of less than 10 nm were applied in all AFM measurements. The scanning rate and scanning scale were 1 Hz and $5.0 \times 5.0 \mu\text{m}^2$ (256 pixels per line), respectively. The recorded original data were analyzed using the AFM system software (NanoScope Analysis, V 1.40) for the determinations of two-dimensional (2D) height image, three-dimensional (3D) oblique image, cross-sectional profile, as well as average roughness (R_a) and root-mean-square (RMS) roughness. In addition, the surface morphologies within $722.1 \times 962.8 \mu\text{m}^2$ were tracked using a 3D noncontact interferometric microscope (ContourGT-K0, Bruker).

The mass difference of the wafers before and after polishing was determined by an analytical electron balance (XS105, Mettler Toledo, exact to 0.01 mg). Polishing efficiency or material removal rate (RR , nm/min) was defined as the thickness difference before and after polishing in unit time, and calculated as follows: $MRR = \Delta m/pts$. Herein, Δm is the mass discrepancy of the workpieces before and after finishing, ρ is the density of SiO_2 layer (2.2 g/cm^3), s is the substrate area, t is the polishing time. In this work, the presented roughness and RR data were the average of three runs.

3. Results and discussion

3.1. Structural analyses of heterostructures

The crystal structure and phase purity of the pure and Y-doped CS/ CeO_2 were analyzed by XRD. The characteristic diffraction peaks (**Fig. 2**) of the samples locate at ca. 28.4°, 47.5°, 56.5°, 69.2°, and 77.7°, corresponding to the lattice planes of (111), (220), (311), (400), and (331) of cubic fluorite-type CeO_2 (JCPDS No. 34-0394) [46]. It indicates that the CeO_2 is highly crystalline and also matches the results observed

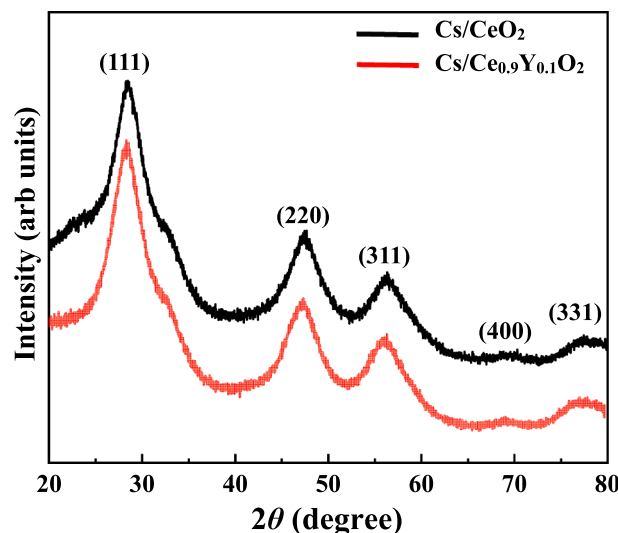


Fig. 2. XRD patterns of pure and Y-doped CS/ CeO_2 hybrids.

by HRTEM. For the Y-doped products, the XRD peaks ascribed to yttrium oxides (Y_2O_3) can hardly be detected, revealing that the dopant cations have been well inserted into the CeO_2 host lattices. In addition, the CeO_2 and CeYO_2 nanocrystal sizes calculated from the Scherrer formula ($d = K\lambda/\beta \cos \theta$) are ca. 5.47 nm and 5.33 nm, respectively. The lattice parameters of the resulting hybrids were further determined from X-ray line broadening of the (111) diffractions using the Scherrer's equation. And the calculated data for the pure and Y-doped CeO_2 are ca. 5.44 Å and 5.41 Å, respectively. Ionic radius of Y^{3+} (0.90 Å [28]) is slightly smaller than that of Ce^{4+} (0.97 Å [29]), hence a lattice contraction is expected due to the incorporation of Y^{3+} in CeO_2 lattices. Furthermore, the typical broad peak at ca. $2\theta = 22^\circ$ – 23° assigned to amorphous materials (JCPDS No. 29-0085) cannot be clearly found from the XRD patterns, implying the CeO_2 nanocrystals locate on CS surfaces and the well-defined core/shell structure formations.

FT-IR characterization over CS/ CeO_2 was carried out to analyze the infrared absorption characteristics. As shown in Fig. 3, the peak at ca. 3435 cm^{-1} can be attributed to the stretching vibration of O—H (hydroxyl or carbonyl groups), and the peak at ca. 1620 cm^{-1} corresponds to C=C stretching of the aromatic carboxylic moiety due to the aromatization of glucose during hydrothermal treatment [47]. The peak appearing at ca. 1384 cm^{-1} may belong to the Ce—O—C stretching vibration [48], implying the formation of the chemical bonds between CeO_2 and Cs. In addition, the absorption peak at ca. 701 cm^{-1} can be ascribed to the Ce—O—Ce vibration [49], and another weak peak at ca. 486 cm^{-1} can be assigned to the Ce—O vibration [50]. These IR results are in accordance with the XRD analyses (Fig. 2).

The intuitive morphology and particle size of bare CS and hybrids were examined by SEM and TEM observations. As shown in Fig. 4a, SEM image clearly reveal that CS samples are spherical and polydispersed with mixed particle sizes. Typically, the CS products exhibit three kinds of particle diameters, namely, relatively small spheres (70–80 nm), medium-sized spheres (140–150 nm), and relatively large spheres (250–260 nm). The corresponding DLS result (Fig. 4b) further confirmed the relatively broad particle-size distribution ranged from 50 nm to 300 nm, which also accord with the SEM observations. As shown in Fig. 4c and e, the provided SEM images indicate that the resulting pure and Y-doped CS/ CeO_2 hybrids maintain good sphericity, and present relatively rough appearances compared to the bare CS. The microstructures, nanocrystalline properties, and direct evidences of the core/shell architectures were further confirmed from TEM observations over the pure and Y-doped CS/ CeO_2 . The TEM images of Fig. 4d and f reveal a reduced electronic contrast around the Cs cores by comparison with the dense

shells (10–15 nm in thickness), which also proves the existence of the core/shell structures of the hybrids. It may be attributed to the weaker absorption of electron beams of amorphous CS materials than that of inorganic compounds. From the HRTEM images inset in Fig. 4d and f, the lattice spacings of pure and Y-doped CeO_2 are ca. 0.33 nm and 0.31 nm respectively, which can correspond to the (111) planes of the cubic fluorite phase CeO_2 crystals. Due to the smaller ionic radius of Y^{3+} than that of Ce^{4+} , the Y^{3+} ions may occupy the lattice sites of the Ce^{4+} ions and form Y-doped CeO_2 nanocrystals. Consequently, the CeYO_2 nanocrystals exhibit a slightly reduced lattice spacing for the (111) planes compared to the pristine CeO_2 .

In order to explore the charge separation and transfer properties, PL spectra of the commercial CeO_2 NPs, CS/ CeO_2 , and CS/ CeYO_2 samples were recorded using a He-Ne laser source with excitation wavelength of 325 nm. A lower PL emission intensity commonly indicates a lower recombination rate or higher separation efficiency of photo-generated carriers. It is well known that high photochemical/photocatalytic oxidation activity can be attributed to the excellent separation efficiency of photo-induced electron-hole pairs. For CeO_2 materials, the PL emission bands in a range of 400–500 nm are related to the different defect levels (Vo, dislocation, etc.) of the range from Ce 4f to O 2p band [51]. As shown in Fig. 5, the commercial CeO_2 displays a strong PL emission peak at ca. 447 nm, indicating a high recombination rate of photo-excited pairs. Conversely, the excited pure and Y-doped CS/ CeO_2 hybrids under the same conditions exhibit a significantly reduced intensity of the PL emission peaks, revealing that the photo-electrons generated by CeO_2 or CeYO_2 can quickly migrate to CS materials. Furthermore, the CS/ CeYO_2 hybrids illustrate a lower room-temperature PL intensity compared to the undoped ones. It verifies that Y-doping treatment contributes to the charge separation and transfer enhancements, which may be responsible for the improved photooxidation activity of the functional CS/ CeYO_2 abrasives in PCMP.

The Raman spectra of pure and Y-doped CS/ CeO_2 hybrids can be found in Fig. 6. The peaks at ca. 1350 cm^{-1} may be attributed to the D-band resulted from the sp³ hybridization of carbon materials [52,53]. The strong peaks at ca. 1590 cm^{-1} can be ascribed to the G-band (graphitic layer) related to sp² vibrations of carbon materials [52,53]. The presences of D and G bands further confirm the successful combination of CS with CeO_2 . In addition, the enlarged Raman spectra with a wavenumber range of 300–700 cm^{-1} are also inserted in Fig. 6a and b. The peaks at 455 – 459 cm^{-1} correspond to the typical Raman vibration mode (F_{2g}) of the cubic fluorite-type CeO_2 materials [54]. It is noteworthy that the peak of F_{2g} mode slightly shift to the low wavenumber after Y-doping, which may be attributed to be a consequence of the increase of Ce^{3+} concentration [54,55]. The peaks at 576 – 587 cm^{-1} can also be associated with structural defects of CeO_2 materials (typically Vo). Herein, the peak intensity of the band at 455 – 459 cm^{-1} and 576 – 587 cm^{-1} are denoted as I_1 and I_2 , respectively. It is commonly recognized that the ratio of I_2/I_1 can reflect the concentration of Vo resulting from the presence of Ce^{3+} in CeO_2 systems [54,55]. The calculated I_2/I_1 value for CS/ CeYO_2 (ca. 0.20) is obviously higher than that of CS/ CeO_2 (ca. 0.09), suggesting the Vo enrichment after Y-doping in CeO_2 lattices. In summary, the provided results clearly indicate that the CS/ CeYO_2 hybrids exhibit more surface defects (Ce^{3+} and Vo) by comparison with the undoped ones, which are effective in both photochemical and tribochemical activity enhancements.

The surface chemical composition and valence states of CS/ CeO_2 products were analyzed by XPS spectroscopy. The recorded XPS survey spectrum (Fig. 7a) confirms the presence of Ce, O, and C elements. The high-resolution Ce 3d core level spectrum further reveals the coexist of Ce^{3+} and Ce^{4+} species at CeO_2 surfaces. Moreover, the peaks centered at ca. 900.5 eV and 882.0 eV can be attributed to the Ce^{3+} contributions, and the peaks at ca. 916.2 eV and 898.0 eV can be assigned to the Ce^{4+} contributions. The Ce 3d electron core level and two group peaks (denoted as v and u) obtained after deconvolution treatment are displayed in Fig. 7b. The labels of (u_0, v) , (u'', v'') and (u''', v''') can be

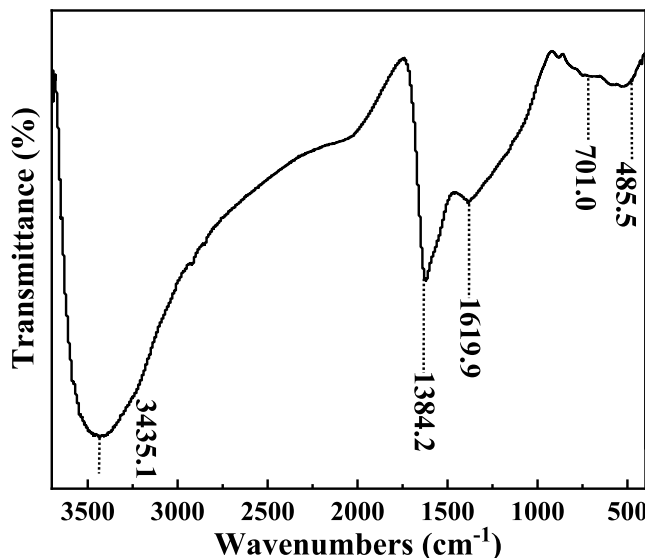


Fig. 3. FT-IR spectra of CS/ CeO_2 samples.

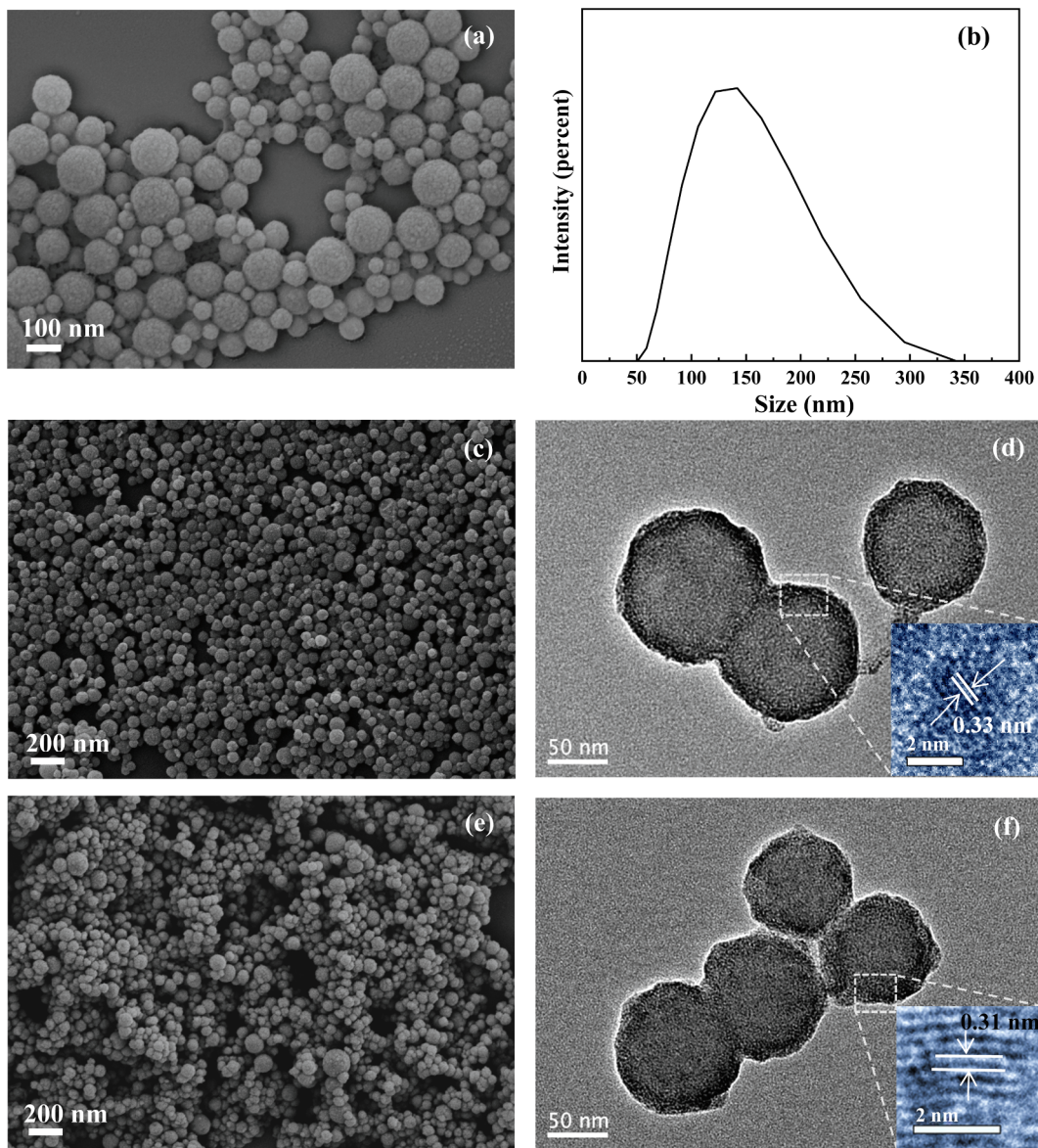


Fig. 4. FESEM, TEM, HRTEM (inset) images and particle-size distribution of (a, b) CS, (c, d) CS/CeO₂, (e, f) CS/CeYO₂ products.

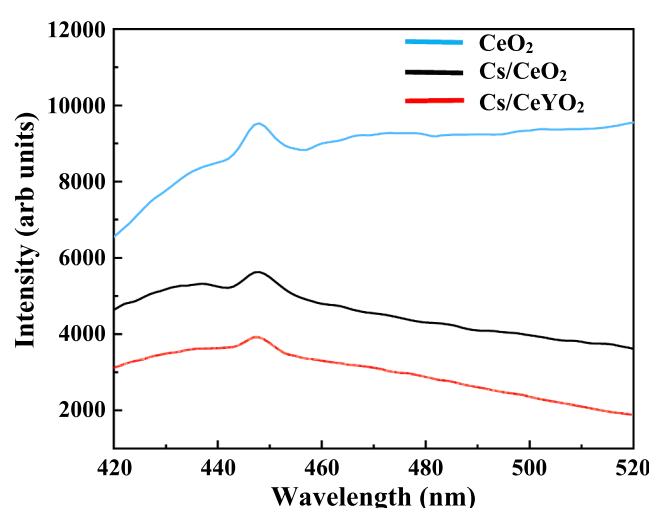


Fig. 5. PL spectra of the commercial CeO₂ NPs, CS/CeO₂, and CS/CeYO₂ samples.

classified as Ce 3d_{5/2} and Ce 3d_{3/2} related to Ce⁴⁺, originating from the final states of Ce (3d⁹4f⁰) O (2p⁶), Ce (3d⁹4f¹) O (2p⁵) and Ce (3d⁹4f²) O (2p⁴), respectively. Two pairs of doublets, (u, v_0) and (u', v'), for the Ce 3d bond energy peak can be ascribed to Ce³⁺, and the double lines correspond to Ce (3d⁹4f¹) O (2p⁶) and Ce (3d⁹4f¹) O (2p⁵), respectively, which are consistent with those reported previously [56,57]. The ratio of valence states of ceria can be semi quantitatively analyzed using the integrated peak areas of the respective valence states.

The data corresponding to the oxidation states, the binding energies, and the peak areas of Ce species are provided in Table 1. In this work, the as-prepared hybrids were annealed under non-oxidizing nitrogen atmosphere. The Ce³⁺ content is as high as ca. 42.6% for the CS/CeO₂ hybrids. In addition, the Vo at CeO₂ surfaces can be correlated the Ce³⁺ in CeO₂ materials and created from the transformation of Ce⁴⁺ → Ce³⁺. Consequently, the high Ce³⁺ content also imply the existence of abundant Vo at surfaces, thus leading to the improved photocatalytic and tribochemical properties.

The high-resolution C1s XPS spectrum (Fig. 7c) can be deconvoluted into five peaks centered at 283.8 eV, 284.4 eV, 284.9 eV, 286.0 eV, and 288.3 eV, respectively. It may be attributed to the graphitic carbon (C—C, CHx), phenolic carbonyl groups (C₆H₅—C₅O), carbonyl and/or

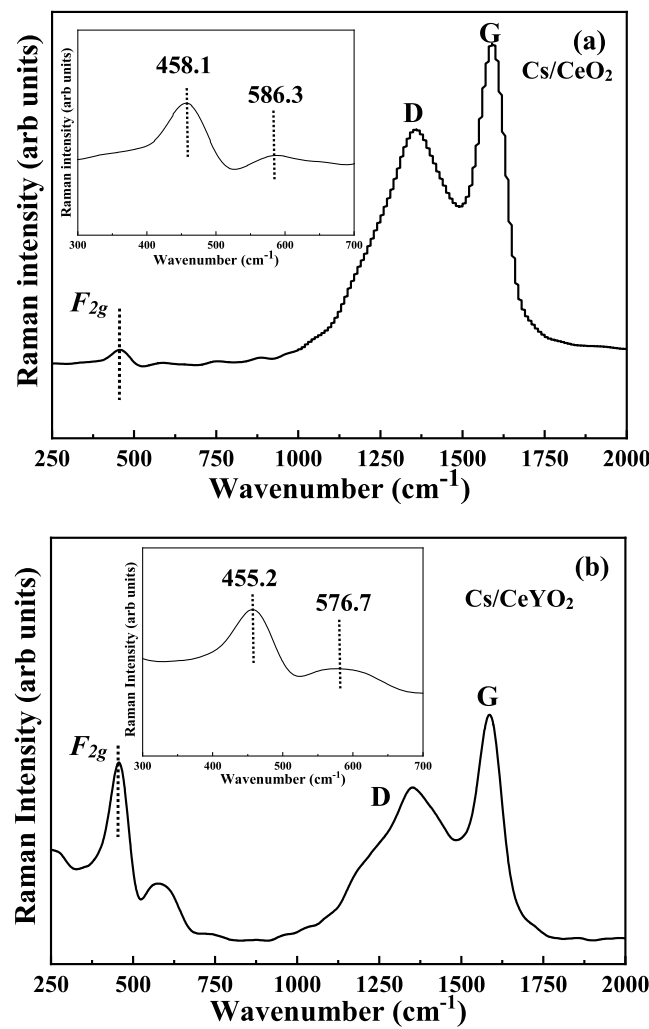


Fig. 6. Raman spectra of (a) CS/CeO₂ and (b) CS/CeYO₂ hybrids.

ester groups (C₅O, —COOR) of carbon materials [58]. These groups could be generated by a series of complicated reactions in Cs formations, including dehydration (e.g., aldol condensation, esterification), decarbonylation, aromatization, etc.

3.2. CMP and PCMP performances

3.2.1. Surface analysis and removal efficiency

High-resolution surface topography and roughness within $5 \times 5 \mu\text{m}^2$, as well as the sectional line-scan profile of the wafers before and after polishing were investigated by AFM. For subsequent comparisons, the diagonals of 2D-AFM height images were selected for the profile measurements. In typical AFM-height images, the bright spots mean the relatively high regions, and the dark points correspond to the relatively low domains. Consequently, the improved color uniformity or reduced color aberration in height images imply the highly planarized surfaces. The representative 2D-AFM height image (Fig. 8a) indicates the rough appearance of the surface prior to finishing. And the average *Ra* and *RMS* roughness were determined to be 1.03 nm and 1.37 nm, respectively. The corresponding cross-sectional profile (Fig. 8b) along the dotted line reveals the maximum peak height (MPH) of 2.9 nm and the maximum valley depth (MVD) of -2.5 nm.

The *Ra* and *RMS* roughness data of three runs over the surfaces after polishing are listed in Table 2. In this work, the developed pure and Y-doped CS/CeO₂ hybrids as functional abrasives achieve ultra-smooth and high-flatness surfaces without distinct defects (scratches, pits,

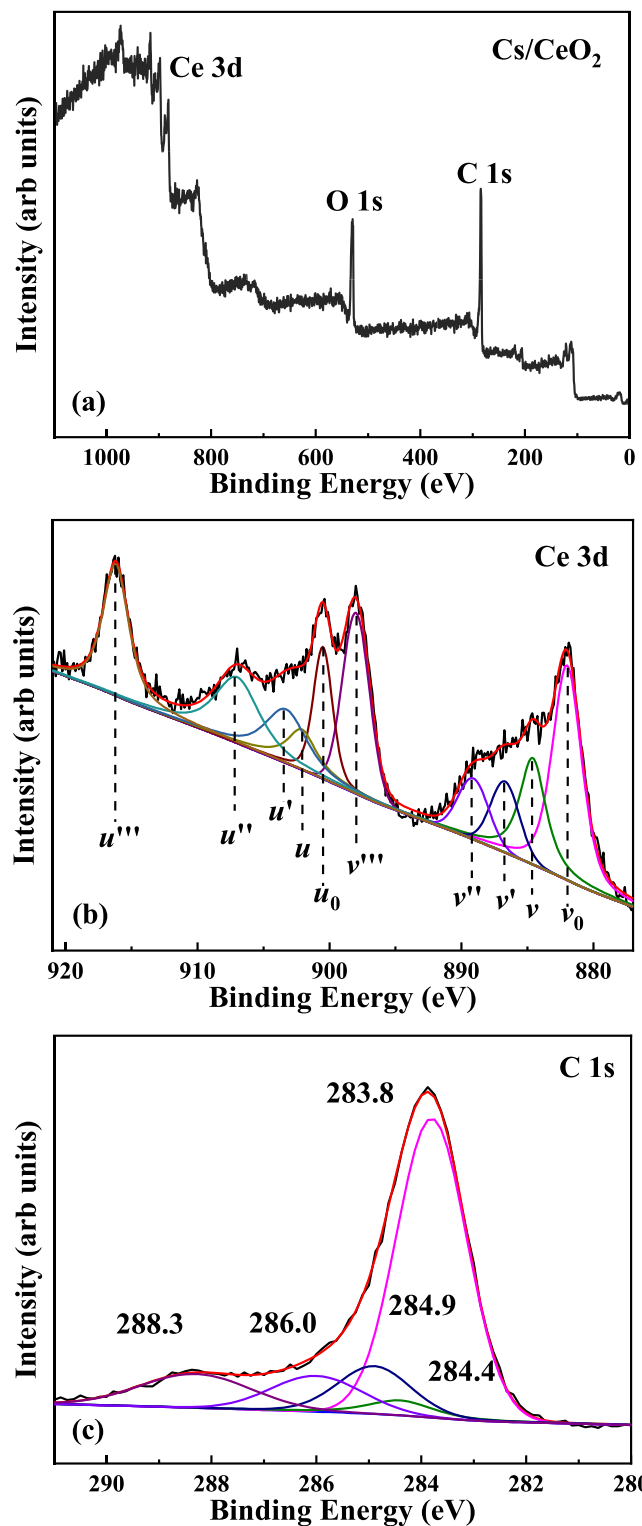


Fig. 7. XPS spectra of (a) full survey spectrum, (b) Ce 3d and (c) C 1s core level spectra for CS/CeO₂ samples.

residues, etc.) in both CMP and PCMP experiments. As shown in Figs. 9–11, the typical 2D-AFM height images of the finished surfaces demonstrate the excellent planeness, uniformity, and homogeneity compared to the original surface (Fig. 8a). For CS/CeO₂ abrasives, the *Ra* and *RMS* roughness obtained under CMP conditions are 0.11 ± 0.01 nm and 0.14 ± 0.01 nm, which are comparable to those achieved under PCMP conditions (0.13 ± 0.02 nm *Ra*, 0.16 ± 0.02 nm *RMS*). After

Table 1

The data of the oxidation states, the binding energies, and the peak areas of Ce species for CS/CeO₂ hybrids.

Ce 3d _{5/2}	v_0 (Ce ³⁺)	v (Ce ⁴⁺)	v' (Ce ³⁺)	v'' (Ce ⁴⁺)	v''' (Ce ⁴⁺)
BE (eV)	882.0	884.6	886.7	889.1	898.0
Area	14167.0	7141.0	3913.0	3509.2	9147.3
Ce 3d _{3/2}	u_0 (Ce ³⁺)	u (Ce ⁴⁺)	u' (Ce ³⁺)	u'' (Ce ⁴⁺)	u''' (Ce ⁴⁺)
BE (eV)	900.5	902.1	903.3	907.0	916.2
Area	5433.2	3385.6	5299.7	7221.7	8474.3

PCMP with CS/CeYO₂ abrasives, the R_a and RMS roughness values decrease to 0.10 ± 0.01 nm and 0.15 ± 0.03 nm, respectively. After conventional CMP, the line-scan profiles (Lines 1 and 2 in Fig. 9) present that the Cs/CeO₂ abrasives enable the topographical variation reduction from -0.26 nm (MVD) to 0.27 nm (MPH). In the case of PCMP, the CS/CeO₂ hybrids achieve the MVD of -0.26 nm and the MPH of 0.29 nm, as verified by the sectional analyses (Lines 3 and 4 in Fig. 10). After PCMP with CS/CeYO₂ abrasives, the line traces (Lines 5 and 6 in Fig. 11) exhibit the topographical variation ranged from -0.29 nm (MVD) to 0.29 nm (MPH). An evidently reduced topographical variation also confirms a highly improved surface planarization degree.

As one of the most popular and powerful tools, AFM enables to provide high-resolution surface characteristics (morphology, defect, roughness, profile, etc.) with an angstrom-level accuracy. However, AFM can generally offer the high-resolution images within a relatively small region (typically $\sim 10 \times 10 \mu\text{m}^2$) due to the limited scanning rate. For tracking large-scale surface morphologies, the finished substrates were further examined using a 3D noncontact interferometric microscope within a scanning range of $722.1 \times 962.8 \mu\text{m}^2$. As shown in Fig. 12, the microscopic defects such as mechanical scratches, etching pits, residual particles, etc. can hardly be detected, also confirming the good surface quality after CMP and PCMP. These results clearly confirm that both CS/CeO₂ and CS/CeYO₂ abrasives can reach surface roughness and topography variation within atom dimension, revealing the

application potentials in achievements of ultra-precise and damage-free polishing.

A comparison of 3D-AFM oblique images can provide direct evidences over the surface morphology changes produced by CMP and PCMP. As shown in Fig. 13a, numerous nano-sized asperity peaks can be clearly observed from the surface prior to finishing. After CMP or PCMP with hybrid abrasives (Fig. 13b-d), most nano-asperities were effectively removed, and the surfaces were highly planarized without introducing new mechanical and/or chemical defects, thus leaving high-quality ultra-smooth surfaces.

Polishing efficiency or removal rate RR is another key evaluating indicator for a successful polishing. Fig. 14 shows the average RR data achieved by pure and Y-doped CS/CeO₂ abrasives under CMP and PCMP conditions. In this work, the CS/CeO₂ abrasives offer an average RR-PCMP of 110 ± 17 nm/min (with UV irradiation), leading to a ca. 134% increase compared to RR-CMP (47 ± 13 nm/min, without UV irradiation). In addition, the Y-doped CS/CeO₂ abrasives offer another ca. 26% enhancement of RR-PCMP (139 ± 11 nm/min) with respect to the undoped ones. Introduction of UV irradiation and/or Y-doping contributes to the RR enhancements for the developed CS/CeO₂ functional abrasives. Herein, we compare the as-proposed CS/CeO₂ abrasives to the previously reported ones over silica wafers under comparable polishing conditions. And the average RR and surface roughness (within $5.0 \times 5.0 \mu\text{m}^2$) data are summarized in Table 3. Among these porous and core/shell abrasives, the developed CS/CeO₂ hybrid abrasives contribute to the further improvements of surface quality and/or removal efficiency, thus exhibiting superior polishing performance. It may be attributed to the enriched Ce³⁺ and V_O defects, the enhanced tribochemical and/or photochemical activities, as well as the enhanced structure stability.

3.2.2. Possible PCMP mechanism

Fig. 15 shows the proposed schematic diagrams depicting the interfacial contact, surface modification, as well as the material removal between the developed CS/CeO₂ abrasives and the chemically reacted surfaces.

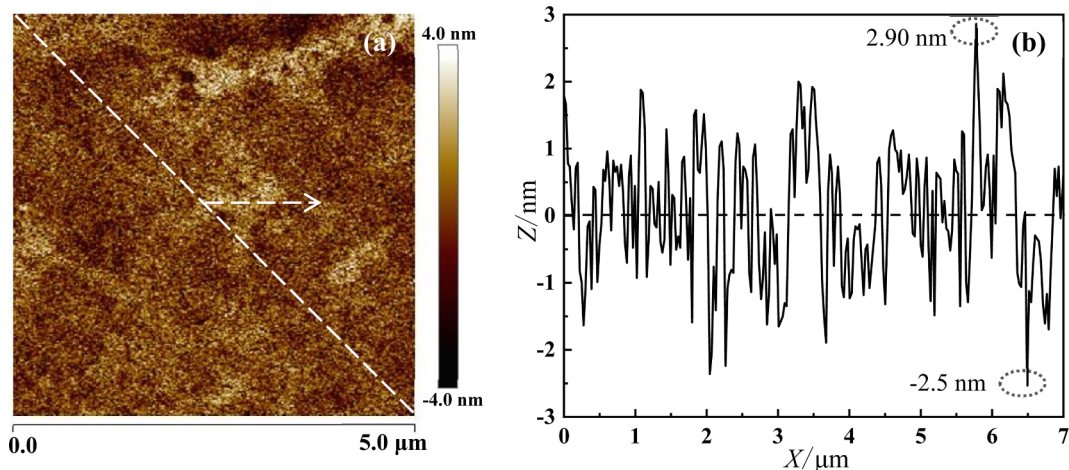


Fig. 8. Typical 2D-AFM image within $5.0 \times 5.0 \mu\text{m}^2$ (a) and the corresponding line-scan profile (b) of the surface prior to polishing.

Table 2

Surface R_a and RMS roughness data achieved by pure and Y-doped CS/CeO₂ abrasives under CMP and PCMP conditions.

Sample	Ra (nm)				RMS (nm)				
	Run 1	Run 2	Run 3	Average Ra	Run 1	Run 2	Run 3	Average RMS	
Cs/CeO ₂	CMP	0.114	0.113	0.103	0.11 ± 0.006	0.143	0.143	0.130	0.14 ± 0.008
	PCMP	0.114	0.114	0.149	0.13 ± 0.020	0.146	0.146	0.188	0.16 ± 0.024
Cs/CeYO ₂	PCMP	0.102	0.103	0.109	0.10 ± 0.004	0.129	0.188	0.138	0.15 ± 0.031

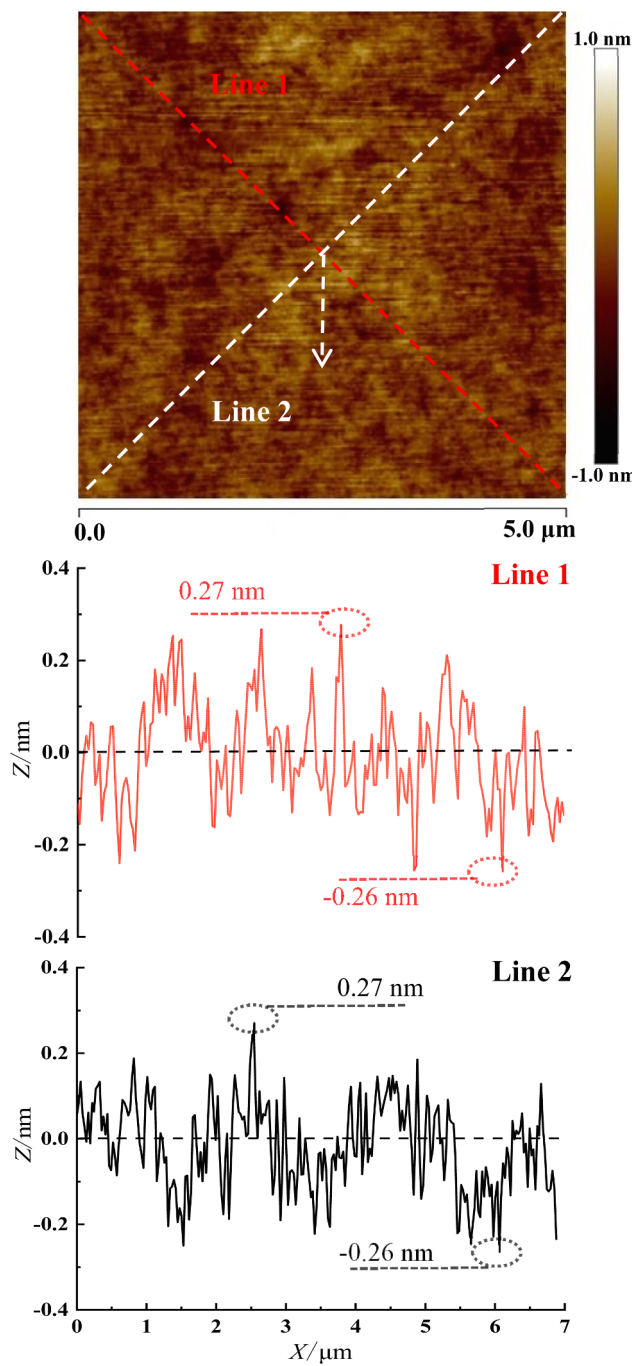


Fig. 9. Typical 2D-AFM image within $5.0 \times 5.0 \mu\text{m}^2$ and the corresponding line-scan profiles of the surface after CMP with CS/CeO₂ abrasives.

In ultra-precise grinding and polishing, experimental and theoretical investigations clearly confirm that the physicochemical properties of abrasives highly affect the interfacial contact state, material removal behavior, surface quality, and polishing rate. Compared to conventional rigid inorganic abrasives, the flexible or non-rigid core/shell abrasives [17,19,21–24,36,41–44,59] and porous abrasives [60–65] with significantly reduced moduli contribute to the contact stress and indentation depth reductions, as well as the contact area enlargement between particles and surfaces, thereby leading to the surface defect/damage elimination and surface quality improvement. The abundant internal pore structures can be responsible for the non-rigid mechanical characteristics of porous abrasives. For the core/shell composites with a thin shell [66–71], the elastic response and compressive modulus may be

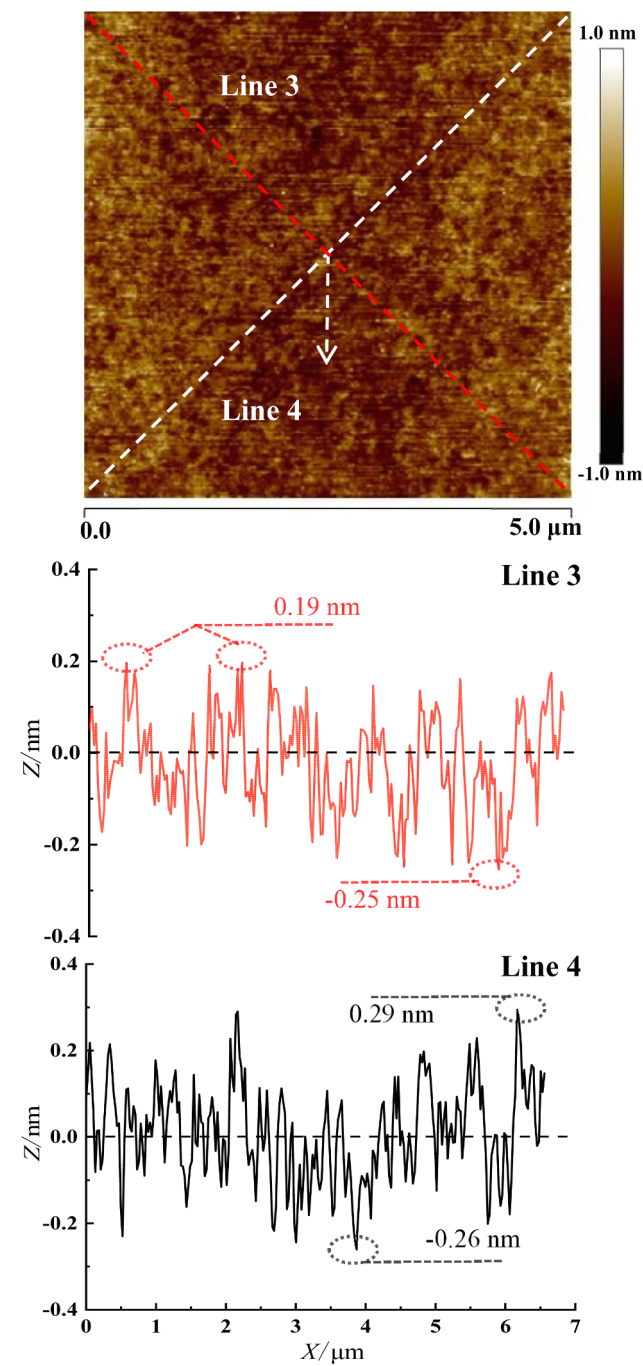


Fig. 10. Typical 2D-AFM image within $5.0 \times 5.0 \mu\text{m}^2$ and the corresponding line-scan profiles of the surface after PCMP with CS/CeO₂ abrasives.

mainly affected and determined by their involved cores. Ozden and coworkers [72] explored the stiffness and elastic modulus of B and N codoped carbon-based nanospheres (CNS, 50–250 nm) produced using a chemical vapor deposition approach. Nanomechanical compressions on individual CNS spheres were conducted via a Hysitron *in-situ* SEM apparatus (PI 85 PicoIndenter), and the elastic modulus of 33.3 GPa was calculated using unloading curves. For bulk CeO₂ materials, the high elastic moduli of 249–264 GPa [73,74] were determined through experimental measurement and theoretical calculation methods. As confirmed by TEM and SEM observations, the proposed CS/CeO₂ hybrids possess a thin CeO₂ shell (ca. 10 nm in thickness), which is much smaller than the particle size of Cs cores (typically 80–260 nm). On the basis of the discussion mentioned above, we can safely assume that the

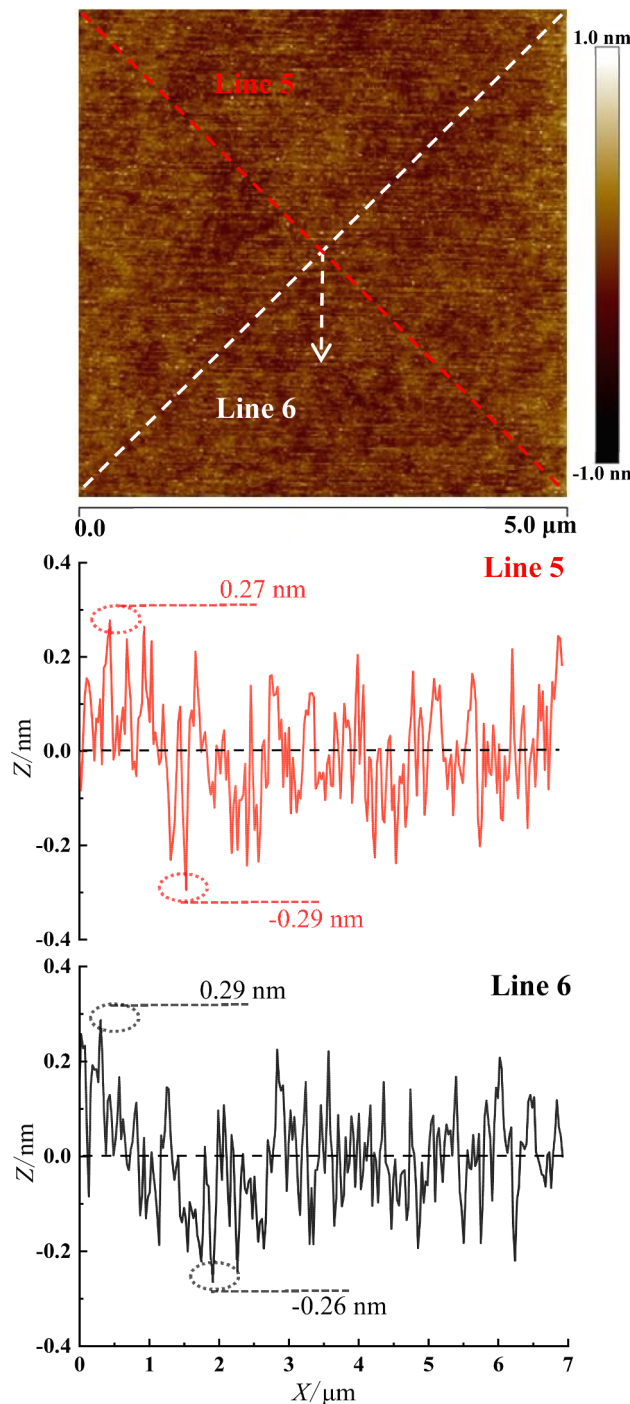


Fig. 11. Typical 2D-AFM image within $5.0 \times 5.0 \mu\text{m}^2$ and the corresponding line-scan profiles of the surface after PCMP with CS/CeYO₂ abrasives.

CS/CeO₂ composite particles exhibit a reduced overall modulus compared to rigid CeO₂ ones, thereby revealing non-rigid mechanical properties.

As shown in Fig. 15a, the slightly elastic deformation of the non-grid CS/CeO₂ hybrids might occur under an applied down pressure during CMP and PCMP processes. It can be expected to achieve the larger contact area and the lower but more uniform stress distribution over the substrate surface. In addition, the spring-like CS/CeO₂ composites might easily adapt to the polishing pad asperities, hence contributing to the topography variation reduction and surface planarization improvement. Consequently, the nearly damage-free polishing can be achieved by CS/CeO₂ abrasives, resulting from the uniform material removal and the

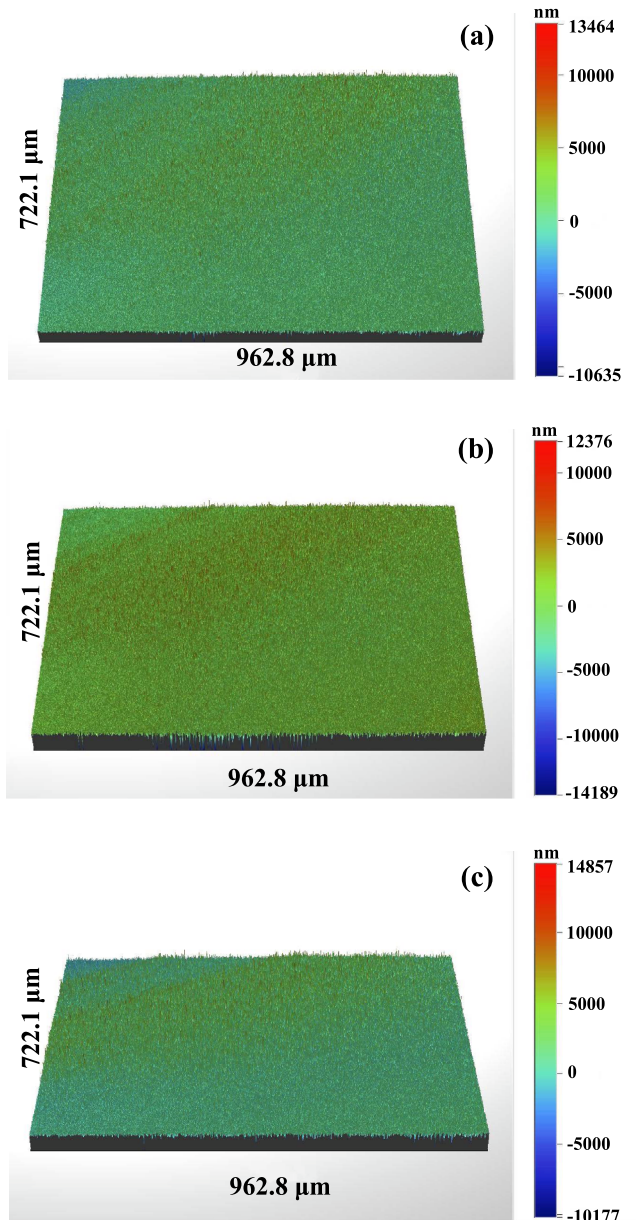


Fig. 12. Morphologies within $722.1 \times 962.8 \mu\text{m}^2$ of the surfaces after (a) CMP and (b) PCMP with CS/CeO₂, and PCMP with (c) CS/CeYO₂ abrasives.

optimization of physical microcontact behavior [36,75–78].

In a typical oxide removal process, the SiO₂ films were firstly corroded and softened by the chemical components in slurries. Subsequently, the chemically reacted layers were removed through the mechanical (or tribochemical) actions of the particle abrasives in slurries. In weakly alkaline polishing conditions, the SiO₂ films reacted with OH⁻ in aqueous solutions, thus leading to the formations of Si—OH bonds and hydration layers. Consequently, the oxide RR can be highly affected by the dynamic formation and removal of the softened corrosion products (typically hydrated layers) [78]. As shown in Fig. 15b, the grafted CeO₂ NPs in the shells absorb the photon energy from UV irradiation during PCMP processes, and then can be excited and produce photogenerated electron-hole ($e^- - h^+$) pairs. The photoinduced carriers can react with the surrounding environment to produce oxidation-active groups [30–32], such as h^+ , hydroxyl radical (OH), superoxide radical (O₂[·]), etc. These active species in polishing slurries are expected to provide extra and strong oxidizing activities, thus accelerating the formation of chemically reacted layers. It is commonly recognized that an improved oxidation

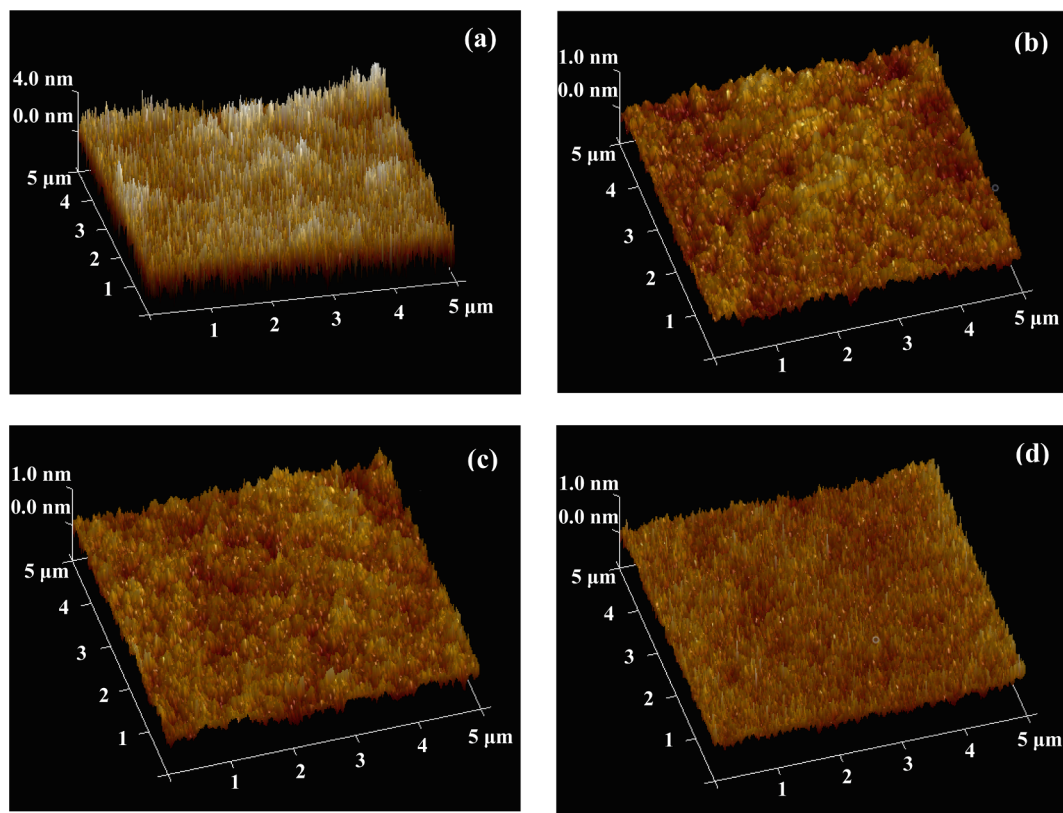


Fig. 13. Typical 3D-AFM oblique images of the surfaces (a) before and after (b) CMP and (c) PCMP with CS/CeO₂, and after PCMP with (d) CS/CeYO₂ abrasives.

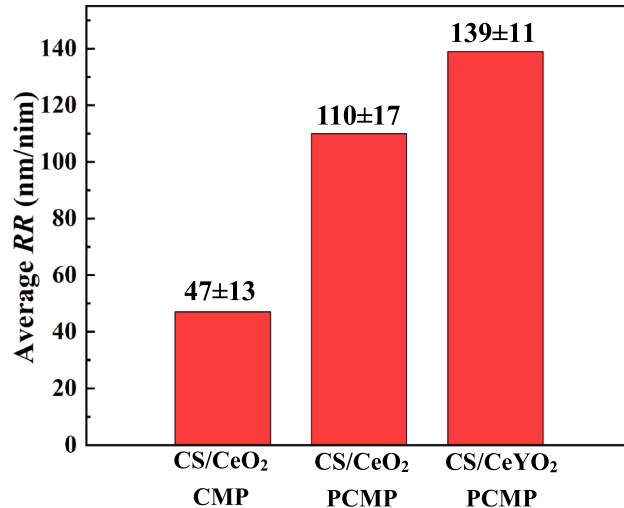


Fig. 14. Average RR data achieved by pure and Y-doped CS/CeO₂ abrasives under CMP and PCMP conditions.

activity of polishing slurries contributes to the easily removed layer formation and thereby lead to an enhanced oxide RR. Consequently, the developed CS/CeO₂ functional abrasives achieve an obviously enhanced oxide-RR in PCMP conditions than that of CMP tests, possibly resulting from the enhanced oxidation and/or corrosion activities of polishing slurries. The photochemical oxidation mechanism of CS/CeO₂ hybrids will be discussed in detail subsequently.

For the oxide films polished with CeO₂ abrasives, the material removal involves the multi-step process of the formation and breakage of Ce(III)—O—Si bonds, which can be interpreted via the chemical tooth mechanism (solid-state tribochemical mechanism) proposed by Cook

Table 3

Summary of the RR and surface roughness (within 5.0 × 5.0 μm²) data over silica wafers.

Abrasives	Average roughness (nm)		Average RR (nm/min)	Reference
	Ra	RMS		
mSiO ₂ /CeO ₂	/	0.17–0.18	38–66	[43]
mSiO ₂ / Ce _{0.83} Er _{0.17} O ₂	/	0.16	71–99	[43]
PS/PANI/CeO ₂	0.12	0.16	81	[44]
PS/CeO ₂	0.11	0.15	26	[59]
D-mSiO ₂ /CeO ₂	0.15	0.18	85	[59]
PS/D-mSiO ₂	/	0.26	72	[60]
PS/W-mSiO ₂	/	0.19	62	[61]
W-mSiO ₂	0.14–0.19	/	34–84	[62]
D-mSiO ₂	0.17–0.24	0.21–0.30	/	[65]

[79] and Hoshino [80]. As shown in Fig. 15c, the water-associated tribochemical reaction might occur at CeO₂—SiO₂ interfaces [81], in which CeO₂ could react with the Si—O[−] sites at the hydration layers of SiO₂ surfaces to create temporary Ce(III)—O—Si bonds. Recently, the adhesion energy between CeO₂ and SiO₂ at different Ce³⁺ contents was investigated by AFM force–curve technique [82]. It was confirmed that an increased Ce³⁺ concentration at CeO₂ NPs surfaces led to the enhanced adhesion energy and interaction of CeO₂—SiO₂. Subsequently, the relative-weak Si—O—Si bonds could be ruptured through the relative motion and the mechanical action between particle abrasives and hydrated layers, thus leading to the effective material removal during CMP/PCMP.

Fig. 16a presents the schematic representation of the photooxidation mechanism toward CS/CeO₂ hybrids. In a typical photochemical (or photocatalytic) system, the semiconductor materials are irradiated with UV light which causes excitation of an e[−] from the valence band (VB) to the conduction band (CB). It can produce an oxidizing site (h⁺) in the VB and a reducing site (e[−]) in the CB. For the CS/CeO₂ systems, the

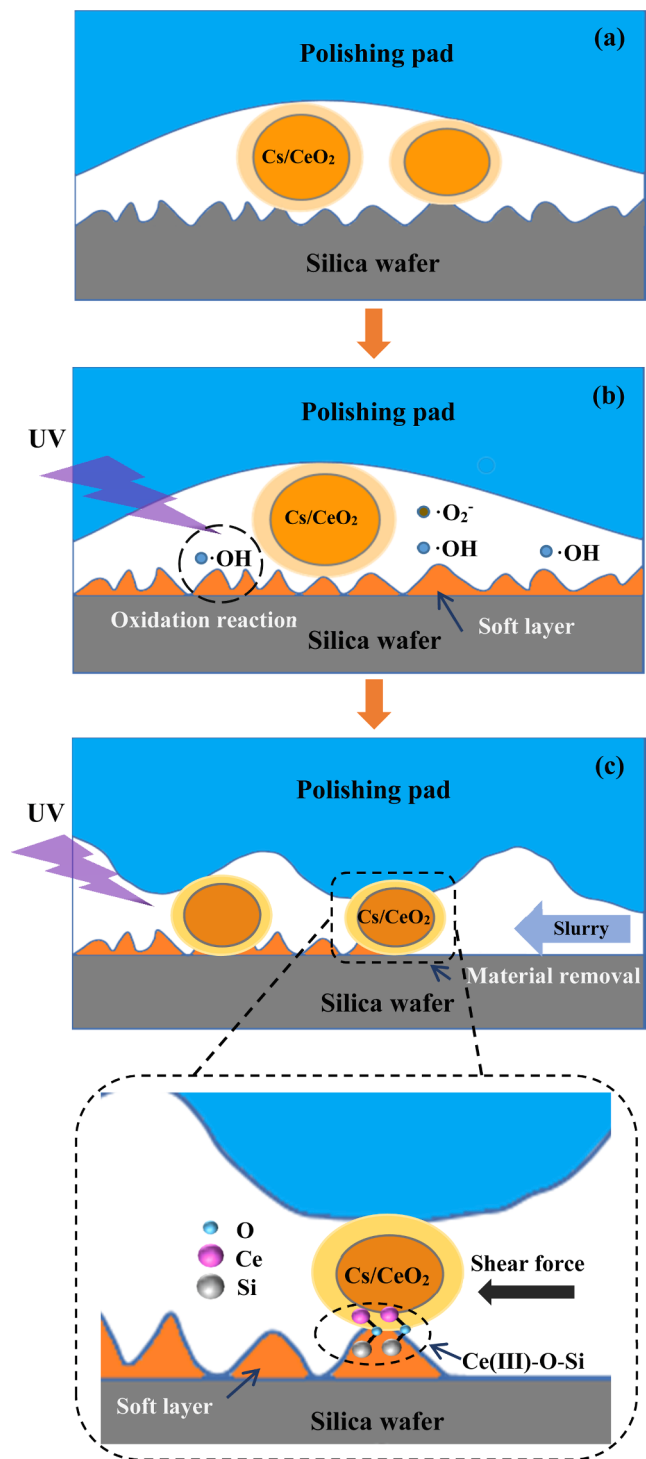


Fig. 15. Schematics of (a) the interfacial contact, (b) the surface modification, (c) the material removal during CMP/PCMP processes using CS/CeO₂ functional abrasives.

photogenerated e^- in the VB of CeO₂ will migrate to CB of CeO₂, and the photoinduced h^+ can be generated in the VB and left on CeO₂ surfaces. The produced h^+ can further react with OH⁻ and H₂O, thus generating strong oxidation ·OH radicals. In addition, the excited e^- can also react with oxygen and/or hydrogen peroxide, hence producing ·O₂ and ·OH active species. It is commonly recognized that the effective separation of e^-/h^+ pairs will play a key role in the enhancement of photochemical (or photocatalytic) oxidation activity. For the developed CS/CeO₂ hybrids, the recombination of e^- and h^+ carriers can be effectively inhibited via

additional charge transfer pathways [30–32]. The conductive CS skeletons will provide a flow channel for the photoexcited e^- from CeO₂ and prolong the lifetime of photoinduced charges.

For amorphous CS materials, it can be speculated that the electronic Fermi level is pinned between the Highest Occupied Molecular Orbital (HOMO) level and the Lowest Unoccupied Molecular Orbital (LUMO) level [83]. The e^- in the CB of CeO₂ can be easily transferred to Cs surfaces due to the good conductivity and the presence of structure defects of Cs materials. And the h^+ can also be migrated from the HOMO of CS to the VB of CeO₂, and can directly participate in the formation of ·OH radicals. Moreover, the charge transfer may not be prone to recombination because the LUMO level of CS may lie above the VB of CeO₂ [84]. The formed built-in electronic field contributes to the fast charge transfer and the photoinduced e^-/h^+ separating efficiency. Moreover, the accumulated e^- at Cs can interact with dissolved oxygen to form ·O₂ radicals, which may also readily react with water to produce H₂O₂. In addition, the photooxidation and photoreduction of H₂O₂ may occur at CeO₂ surfaces. Herein, the photooxidation of H₂O₂ will create ·OOH and H⁺ species, while the photoreduction of H₂O₂ will produce ·OH and OH⁻ species. Such reactions will accelerate the effective separation of photoinduced e^-/h^+ pairs. Consequently, the combination of CS and CeO₂ contributes to the promotion of photogenerated e^- transportation, thus achieving the effectively suppressed recombination rates of photoexcited e^-/h^+ carriers as verified by PL spectra (Fig. 5). The improved photooxidation activity can be responsible for the oxidation active species (h^+ , ·OH, ·O₂, etc.) enrichments in polishing slurries, thus promoting the formation of chemically reacted layer and then enhancing the material removal during PCMP.

In the Y-doped CeO₂ material systems [28,29], Y ions can create impurity level in the forbidden band of CeO₂. This strategy aims to create an acceptor level below the CB of CeO₂ and facilitate the down-hill flow of electron to the dopant level from the CeO₂ CB, then suppress the photogenerated e^-/h^+ recombination. After incorporation of Y³⁺ in CeO₂ lattices, the surface exposed cerium ions are partly substituted by Y³⁺ cations. The as-created Vo [27–29,52,85] can efficiently capture electrons in the CB and restrict the recombination rate of photogenerated chargers in the Y-doped CeO₂. Consequently, the CS/CeYO₂ hybrids present an improved photooxidation activity.

Fig. 16b shows the schematic diagram depicting the atomic structure of the Y-doped CeO₂ surface. Engineering surface defects (typically Vo and Ce³⁺) is one of the most popular strategies for improving the physicochemical performance of CeO₂-based materials with mixed valences of Ce⁴⁺ and Ce³⁺. For doped CeO₂ systems [52], the cationic variations in valence or radius commonly result in the enrichments of Vo and Ce³⁺, possibly resulting from the total positive charge and the Vo formation energy reductions over CeO₂. It was further confirmed that the Ce³⁺ species existed at CeO₂ surfaces and formed a thin Ce³⁺ layer with several nm in depth [86,87]. As shown in Fig. 16b, Y-doping modification can create more Vo and Ce³⁺ at the CeO₂ surfaces, which may also play a key role in oxide removal processes.

In-depth investigations [11–16,22,24,43,82,88–93] revealed that the Ce³⁺ ions at CeO₂ surfaces might more easily adsorb and react with the hydrated layers of SiO₂ films compared to Ce⁴⁺ species. Consequently, the involved Ce³⁺ ions at CeO₂ surfaces could be expected to be active sites and bind to the hydration layers. It was also proposed that the Si—O bonds might be weakened by the exposed Ce³⁺ at CeO₂ surfaces, thus facilitating the Ce(III)—O—Si bond formations. It contributed to the improvement of the water-associated solid-state tribochemical reactivity of CeO₂ abrasives, thereby achieving an enhanced material removal toward SiO₂ films. In addition, the V_O created at CeO₂ surfaces could react with water to form surface hydroxyl groups, which further reacted with the Si—O⁻ sites at SiO₂ films to form Ce(III)—O—Si structures. In summary, more Ce³⁺ and/or V_O at CeO₂ abrasive surfaces contributed to promoting the tribochemical activity between CeO₂—SiO₂ and then accelerating the Ce(III)—O—Si bond formations, thereby leading to the enhancement of removal efficiency toward SiO₂.

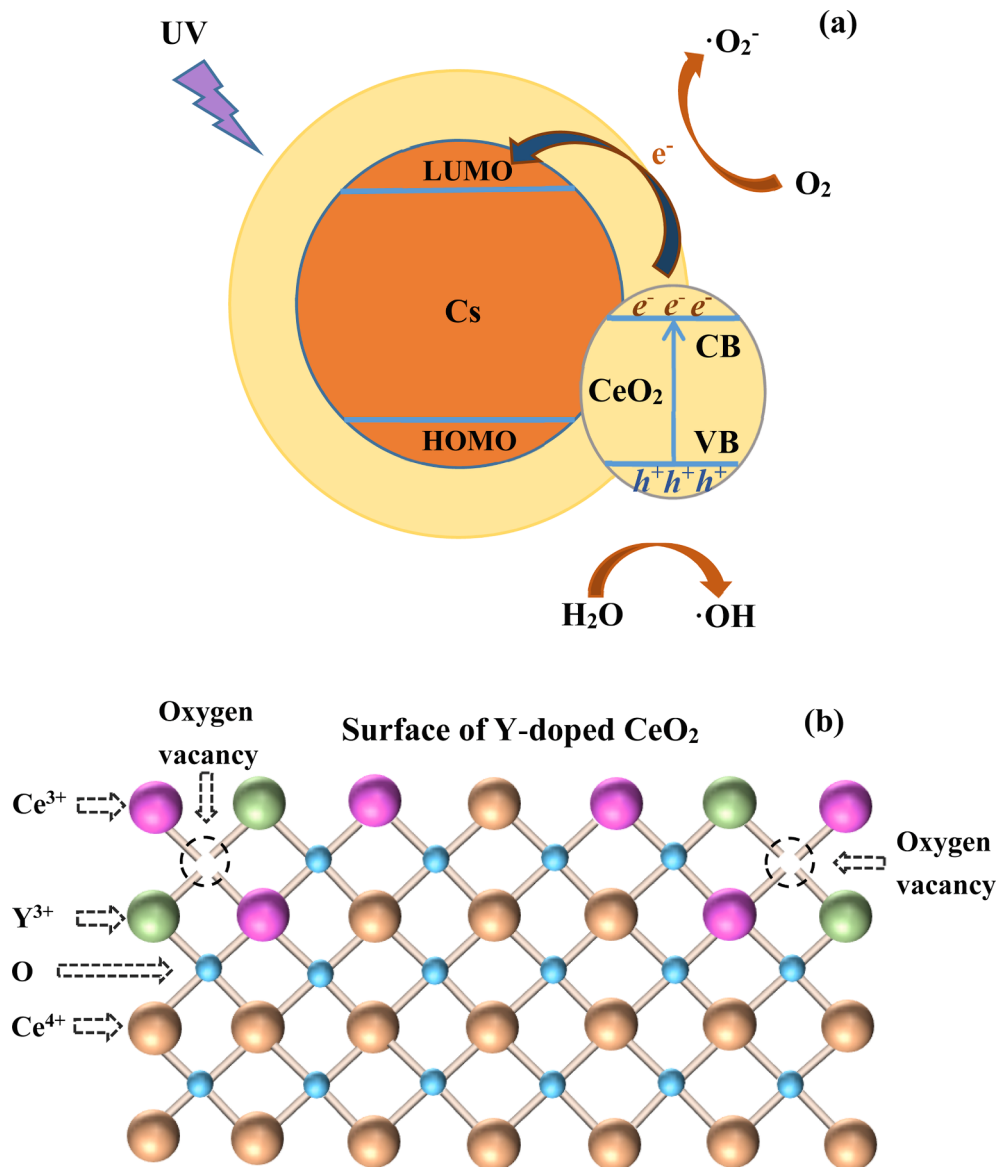


Fig. 16. Schematics of (a) the photooxidation mechanism toward the proposed hybrids and (b) the atomic structure of Y-doped CeO₂ surfaces.

materials.

In this work, Raman spectra (Fig. 6) indicate that Y-doping in CeO₂ lattices creates more structure defects (typically V_O and Ce³⁺) at CeYO₂ surfaces. In photochemical (or photocatalytic) oxidation applications, an appropriate content of V_O in photocatalysts can be expected to be trapping centers for the photoexcited e⁻ or h⁺. It can effectively suppress the recombination and prolong the lifetime of photogenerated chargers, as confirmed by PL spectra (Fig. 5). For the developed CS/CeO₂ materials, the outstanding photooxidation activity may be attributed to the effective separation of photogenerated pairs, resulting from the created CS—CeO₂ heterojunction and the enriched V_O. On the basis of these results, we can conclude that the CS/CeYO₂ hybrids possess an improved photochemical oxidation activity by comparison with the undoped ones. As a result, the CS/CeO₂ functional abrasives can promote the formation of chemically reacted layer during PCMP, and finally contribute to the RR-PCMP improvement. Furthermore, the enriched Ce³⁺ species at CS/CeYO₂ surfaces can act as the active sites and then react with the hydrated layer, thus accelerating the formation and removal of Ce(III)—O—Si bonds between CeO₂—SiO₂ interfaces. The improved of both photochemical and tribochemical reactivities are responsible for the enhancements of formation and removal of chemically reacted layer.

Consequently, the CS/CeYO₂ abrasives allow the RR-PCMP enhancement by comparison with the undoped ones.

Although we have obtained relatively satisfactory consequences in this work, there are still a lot of worthy scientific issues. For example, more direct and solid evidence is needed to explore the intrinsic relationships among the structure feature, mechanical property, surface defect, tribochemistry, photochemistry, and polishing performance of the proposed functional abrasives. In addition, the fundamental understanding of the photooxidation mechanism of CS/CeO₂ materials and the synergistic effect between CS and CeO₂ will be further explored in our group. In order to acquire more information, the relevant studies are under investigation in terms of AFM nano-indentation, *in situ* Raman, *in situ* FT-IR, *in-situ* SEM/TEM compression testing, etc. We believe these results will provide insights into the structure/component optimization, polishing performance improvement, and material removal mechanism of the developed CS/CeO₂ functional abrasives.

4. Conclusions

In summary, this work describes our recent efforts on the design and fabrication of CS/CeO₂ heterostructures as novel functional abrasives

for achieving low-damage and high-efficiency polishing/planarization. As revealed by FESEM and HRTEM, the polydispersed carbon spheres (CS) synthesized via a hydrothermal approach were uniformly coated with a thin pure or Y-doped CeO₂ layer, which was consisted of randomly orientated nanocrystals. The pure and Y-doped CS/CeO₂ hybrids exhibited the strawberry-like appearances with typical core/shell structures. Raman and XPS results showed that Y-doping modification contributed to the tervalent cerium (Ce³⁺) and oxygen vacancy (Vo) enrichments at CeO₂ surfaces, allowing the tribocatalytic activity enhancement. PL spectra clearly confirmed that the created CS–CeO₂ heterojunction was responsible for the efficient separation of photoinduced charges, indicating the photochemical (or photocatalytic) oxidation activity improvement. Under both CMP and PCMP conditions, the CS/CeO₂ hybrids achieved the nearly non-damage surfaces with angstrom-level roughness (0.10–0.13 nm Ra, 0.14–0.16 nm RMS). The involved low-modulus Cs cores might be responsible for the interfacial contact optimization and thus surface quality improvement. Compared to conventional CMP (47 ± 13 nm/min), the CS/CeO₂ hybrids achieved an evidently enhanced RR-PCMP (110 ± 17 nm/min), which was further improved by Y-doping treatment (139 ± 11 nm/min). It might be attributed to the acceleration of the dynamic formation and removal of chemically treated layers, resulting from the tribocatalytic and photochemical activity enhancements. The reduced overall modulus, constructed CS–CeO₂ heterojunction, and manipulated surface defect might be responsible for the improved CMP and PCMP performances of the proposed CS/CeO₂ functional abrasives. This work is expected to offer a promising abrasive system for achieving high-quality and high-efficiency polishing. Moreover, the described strategy can be easily extended to the construction and fabrication of other CS-coupled functional abrasives toward advanced multi-fields assisted polishing (PCMP, ECMP, PECMP, etc.).

CRediT authorship contribution statement

Tianyu Wang: Conceptualization, Methodology, Formal analysis, Investigation, Data curation, Writing – original draft. **Yue Chen:** Validation, Investigation, Software, Data curation. **Ailian Chen:** Formal analysis, Methodology, Visualization. **Yang Chen:** Conceptualization, Resources, Writing – review & editing, Supervision, Project administration, Funding acquisition.

Declaration of Competing Interest

The authors declare that they have no known competing financial interests or personal relationships that could have appeared to influence the work reported in this paper.

Acknowledgements

The work was supported financially by the National Natural Science Foundation of China (Grant Nos. 51575058 and 51875052), and the Priority Academic Program Development of Jiangsu Higher Education Institutions (PAPD).

References

- [1] Z. Zhang, J. Liu, W. Hu, L. Zhang, W. Xie, L. Liao, Chemical mechanical polishing for sapphire wafers using a developed slurry, *J. Manuf. Process.* 62 (2021) 762–771.
- [2] L. Liao, Z. Zhang, F. Meng, D. Liu, B. Wu, Y. Li, W. Xie, A novel slurry for chemical mechanical polishing of single crystal diamond, *Appl. Surf. Sci.* 564 (2021) 150431.
- [3] W. Xie, Z. Zhang, L. Liao, J. Liu, H. Su, S. Wang, D. Guo, Green chemical mechanical polishing of sapphire wafers using a novel slurry, *Nanoscale* 12 (2020) 2518–22526.
- [4] Z. Zhang, Z. Shi, Y. Du, Z. Yu, L. Guo, D. Guo, A novel approach of chemical mechanical polishing for a titanium alloy using an environment-friendly slurry, *Appl. Surf. Sci.* 427 (2018) 409–415.
- [5] Z. Zhang, J. Cui, J. Zhang, D. Liu, Z. Yu, D. Guo, Environment friendly chemical mechanical polishing of copper, *Appl. Surf. Sci.* 467–468 (2019) 5–11.
- [6] Z. Zhang, L. Liao, X. Wang, W. Xie, D. Guo, Development of a novel chemical mechanical polishing slurry and its polishing mechanisms on a nickel alloy, *Appl. Surf. Sci.* 506 (2020) 144670.
- [7] Z. Zhang, Y. Du, S. Huang, F. Meng, L. Chen, W. Xie, K. Chang, C. Zhang, Y. Lu, C. Lin, S. Li, I.P. Parkin, D. Guo, Macroscale superlubricity enabled by graphene-coated surfaces, *Adv. Sci.* 7 (2020) 1903239.
- [8] K. Yuan, X.C. Sun, H.J. Yin, L. Zhou, H.C. Liu, G.H. Yuan, Y.W. Zhang, Boosting the water gas shift reaction on Pt/CeO₂-based nanocatalysts by compositional modification: Support doping versus bimetallic alloying, *J. Energy Chem.* 67 (2022) 241–249.
- [9] M.B. Souza, J.S. Santos, M.S. Pontes, L.R. Nunes, I.P. Oliveira, A.J.L. Ayme, E. F. Santiago, R. Grillo, A.R. Fiorucci, G.J. Arruda, CeO₂ nanostructured electrochemical sensor for the simultaneous recognition of diethylstilbestrol and 17 beta-estradiol hormones, *Sci. Total Environ.* 805 (2022) 150348.
- [10] S. Swathi, R. Yuvakkumar, P.S. Kumar, G. Ravi, M. Thambidurai, C. Dang, D. Velauthapillai, Gadolinium doped CeO₂ for efficient oxygen and hydrogen evolution reaction, *Fuel* 310 (2022) 122319.
- [11] K. Kim, D.K. Yi, U. Paik, Increase in Ce³⁺ concentration of ceria nanoparticles for high removal rate of SiO₂ in chemical mechanical planarization, *ECS J. Solid State Sci. Technol.* 6 (9) (2017) P681–P685.
- [12] C.M. Netzband, K. Dunn, Investigation into the effect of CMP slurry chemicals on ceria abrasive oxidation state using XPS, *ECS J. Solid State Sci. Technol.* 8 (10) (2019) P629–P633.
- [13] J. Cheng, S. Huang, Y. Li, T.Q. Wang, L. Xie, X. Lu, Lu, RE (La, Nd and Yb) doped CeO₂ abrasive particles for chemical mechanical polishing of dielectric materials: Experimental and computational analysis, *Appl. Surf. Sci.* 506 (2020) 144668.
- [14] J. Murata, D. Nagatomo, Investigation of electrolytic condition on abrasive-free electrochemical mechanical polishing of 4H-SiC using Ce thin film, *ECS J. Solid State Sci. Technol.* 9 (2020) 034002.
- [15] E. Kim, J. Hong, S. Hong, C. Kanade, H. Seok, H. Kim, T. Kim, Improvement of oxide removal rate in chemical mechanical polishing by forming oxygen vacancy in ceria abrasives via ultraviolet irradiation, *Mater. Chem. Phys.* 273 (2021) 124967.
- [16] E. Kim, J. Lee, C. Bae, H. Seok, H. Kim, T. Kim, Effects of trivalent lanthanide (La and Nd) doped ceria abrasives on chemical mechanical polishing, *Powder Technol.* 397 (2022) 117025.
- [17] S. Armini, J.D. Messinaecker, C.M. Whelan, M. Moinpour, K. Maex, Composite polymer core-ceria shell abrasive particles during oxide CMP: a defectivity study, *J. Electrochem. Soc.* 155 (2008) H653–H660.
- [18] Z. Zhang, W. Liu, J. Zhu, Z. Song, Synthesis, characterization of ceria-coated silica particles and their chemical mechanical polishing performance on glass substrate, *Appl. Surf. Sci.* 257 (5) (2010) 1750–1755.
- [19] Y. Chen, R. Long, Polishing behavior of PS/CeO₂ hybrid microspheres with controlled shell thickness on silicon dioxide CMP, *Appl. Surf. Sci.* 257 (20) (2011) 8679–8685.
- [20] L. Peedikakkandy, L. Kalita, P. Kavle, A. Kadam, V. Gujar, M. Arcot, P. Bhargava, Preparation of spherical ceria coated silica nanoparticle abrasives for CMP application, *Appl. Surf. Sci.* 357 (2015) 1306–1312.
- [21] Y. Chen, Z. Li, N. Miao, Polymethylmethacrylate (PMMA)/CeO₂ hybrid particles for enhanced chemical mechanical polishing performance, *Tribol. Int.* 82 (2015) 211–217.
- [22] A. Chen, J. Long, Z. Li, Y. Chen, Dependency of structural change and polishing efficiency of meso-silica/ceria core/shell composite abrasives on calcination temperatures, *J. Mater. Sci.: Mater. Electron.* 29 (13) (2018) 11466–11477.
- [23] A. Chen, J. Long, Z. Li, Y. Chen, Copper chemical mechanical polishing performances of polystyrene/ceria hybrid abrasives with a core/shell structure, *J. Inorg. Organomet. Polym.* 28 (4) (2018) 1655–1663.
- [24] Y. Chen, Z. Mu, W. Wang, A. Chen, Development of mesoporous SiO₂/CeO₂ core-shell nanoparticles with tunable structures for non-damage and efficient polishing, *Ceram. Int.* 46 (4) (2020) 4670–4678.
- [25] C. Zhou, X. Xu, L. Dai, H. Gong, S. Lin, Chemical-mechanical polishing performance of core-shell structured polystyrene/ceria/nanodiamond ternary abrasives on sapphire wafer, *Ceram. Int.* 47 (22) (2021) 31691–31701.
- [26] M. Jeyaraj, R. Atchudan, S. Pitchaimuthu, T.N.J.I. Edison, P. Sennu, Photocatalytic degradation of persistent brilliant green dye in water using CeO₂/ZnO nanospheres, *Process Saf. Environ.* 156 (2021) 457–464.
- [27] Y. Li, Q. Wang, G. Zhou, P. Zhao, R. Li, G. Mao, L. Zhang, F. Li, J. Yin, Synthesis of CeO₂ nanoparticles by sacrificial Mg powder with abundant oxygen vacancies and efficiently photocatalytic activity, *Mater. Lett.* 307 (2022) 131075.
- [28] B. Xu, H. Yang, Q. Zhang, S. Yuan, A. Xie, M. Zhang, T. Ohno, Design and Synthesis of Sm, Y, La and Nd-doped CeO₂ with a broom-like hierarchical structure: a photocatalyst with enhanced oxidation performance, *ChemCatChem* 12 (2020) 2638–2646.
- [29] X. Xia, J. Li, C. Chen, Y. Lan, X. Mao, F. Bai, Optimal rare-earth (La, Y and Sm) doping conditions and enhanced mechanism for photocatalytic application of ceria nanorods, *Nanotechnology* 32 (2021) 195708.
- [30] D. Garg, I. Matai, A. Garg, A. Sachdev, Tragacanth hydrogel integrated CeO₂@rGO nanocomposite as reusable photocatalysts for organic dye degradation, *ChemistrySelect* 5 (34) (2020) 10663–10672.
- [31] J. Yao, Z. Gao, Q. Meng, G. He, H. Chen, One-step synthesis of reduced graphene oxide based ceric dioxide modified with cadmium sulfide (CeO₂/Cds/RGO) heterojunction with enhanced sunlight-driven photocatalytic activity, *J. Colloid Interf. Sci.* 594 (2021) 621–634.
- [32] D. Barathi, N. Rajalakshmi, R. Ranjith, R. Sangeetha, S. Meyvel, Controllable synthesis of CeO₂/g-C₃N₄ hybrid catalysts and its structural, optical and visible light photocatalytic activity, *Diam. Relat. Mater.* 111 (2021) 108161.

- [33] Z. Yuan, Y. He, X. Sun, Q. Wen, UV-TiO₂ photocatalysis-assisted chemical mechanical polishing 4H-SiC wafer, *Mater. Manuf. Process.* 33 (11) (2018) 1214–1222.
- [34] J. Lu, Y. Hang, Y. Fu, Q. Yan, S. Zeng, Synergistic Effect of photocatalysis and Fenton on improving the removal rate of 4H-SiC during CMP, *ECS J. Solid State Sci. Technol.* 10 (2021) 044001.
- [35] X. Yu, B. Zhang, R. Wang, Z. Kao, S. Yang, W. Wei, Effect of photocatalysts on electrochemical properties and chemical mechanical polishing rate of GaN, *Mat. Sci. Semicon. Proc.* 121 (2021) 105387.
- [36] B. Gao, W. Zhai, Q. Zhai, Y. Shi, Polystyrene/CeO₂ core/shell abrasives for high-quality 4H-SiC surface in ECMP: The effects of shell thickness, *ECS J. Solid State Sci. Technol.* 9 (2020) 044005.
- [37] X. Yang, X. Yang, K. Kawai, K. Arima, K. Yamamura, Novel SiC wafer manufacturing process employing three-step slurryless electrochemical mechanical polishing, *J. Manuf. Process* 70 (2021) 350–360.
- [38] J. Deng, J. Lu, S. Zeng, Q. Xiong, Q. Yan, J. Pan, Preparation and processing properties of magnetically controlled abrasive solidification orientation—solid-phase Fenton reaction lapping-polishing plate for single-crystal 4H-SiC, *Surf. Interfaces* 29 (2022), 101646.
- [39] M. Uneda, K. Fujii, Highly efficient chemical mechanical polishing method for SiC substrates using enhanced slurry containing bubbles of ozone gas, *Precis. Eng.* 64 (2020) 91–97.
- [40] G. Chen, J. Li, J. Long, H. Luo, Y. Zhou, X. Xie, G. Pan, Surface modulation to enhance chemical mechanical polishing performance of sliced silicon carbide Si-face, *Appl. Surf. Sci.* 536 (2021) 147963.
- [41] B. Gao, W. Zhai, Q. Zhai, M. Zhang, Novel polystyrene/CeO₂-TiO₂ multicomponent core/shell abrasives for high-efficiency and high-quality photocatalytic-assisted chemical mechanical polishing of reaction-bonded silicon carbide, *Appl. Surf. Sci.* 484 (2019) 534–541.
- [42] B. Gao, W. Zhai, Q. Zhai, C. Wang, Novel photoelectrochemically combined mechanical polishing technology for scratch-free 4H-SiC surface by using CeO₂-TiO₂ composite photocatalysts and PS/CeO₂ core/shell abrasives, *Appl. Surf. Sci.* 570 (2021) 151141.
- [43] A. Chen, Y. Han, Z. Mu, W. Cai, Y. Chen, Meso-silica/Erbium-doped ceria binary particles as functionalized abrasives for photochemical mechanical polishing (PCMP), *Appl. Surf. Sci.* 550 (2021) 149353.
- [44] A. Chen, T. Wang, Y. Chen, S. Wang, Y. Chen, Development of polystyrene/polyaniline/ceria (PS/PANI/CeO₂) multi-component abrasives for photochemical mechanical polishing/planarization applications, *Appl. Surf. Sci.* 575 (2022) 151784.
- [45] X. Sun, Y. Li, Colloidal carbon spheres and their core/shell structures with noble-metal nanoparticles, *Angew. Chem. Int. Edit.* 43 (5) (2004) 597–601.
- [46] Y.-C. Huang, S.-H. Wu, C.-H. Hsiao, A.-T. Lee, M.H. Huang, Mild synthesis of size tunable CeO₂ octahedra for band gap variation, *Chem. Mater.* 32 (6) (2020) 2631–2638.
- [47] M. Li, W. Li, S. Liu, Control of the morphology and chemical properties of carbon spheres prepared from glucose by a hydrothermal method, *J. Mater. Res.* 27 (8) (2012) 1117–1123.
- [48] H. Jiang, S. Ge, Y.u. Zhang, M. Liu, J. Zhang, J. Lin, M. Dong, J. Wang, Z. Guo, One-pot microwave-hydrothermally synthesized carbon nanotube-cerium oxide nanocomposites for enhanced visible photodegradation of acid orange 7, *Phys. Chem. Chem. Phys.* 22 (41) (2020) 23743–23753.
- [49] B. Ksapabutr, E. Gulari, S. Wongkasemjith, Sol-gel derived porous ceria powders using cerium glycolate complex as precursor, *Mater. Chem. Phys.* 99 (2-3) (2006) 318–324.
- [50] Z. Yang, Y. Yang, H. Liang, L. Liu, Hydrothermal synthesis of monodisperse CeO₂ nanocubes, *Mater. Lett.* 63 (21) (2009) 1774–1777.
- [51] G. Wang, Q. Mu, T. Chen, Y. Wang, Synthesis, characterization and photoluminescence of CeO₂ nanoparticles by a facile method at room temperature, *J. Alloy Compd.* 493 (1-2) (2010) 202–207.
- [52] R. Rao, R. Podila, R. Tsuchikawa, J. Katoh, D. Tishler, A.M. Rao, M. Ishigami, Effects of layer stacking on the combination Raman modes in graphene, *ACS Nano* 5 (3) (2011) 1594–1599.
- [53] K.N. Kudin, B. Ozbas, H.C. Schniepp, R.K. Prud'homme, I.A. Aksay, R. Car, Raman spectra of graphite oxide and functionalized graphene sheets, *Nano Lett.* 8 (1) (2008) 36–41.
- [54] R. Tao, J. Xu, H. Zhong, W. Wen, Q. Pan, Y. Liu, J. Chen, Finely tuned structure and catalytic performance of cerium oxides by a continuous samarium doping from 0 to 100%, *Inorg. Chem.* 58 (19) (2019) 13066–13076.
- [55] J.H. Park, C.H. Jung, K.J. Kim, D. Kim, H.R. Shin, J.-E. Hong, K.T. Lee, Enhancing bifunctional electrocatalytic activities of oxygen electrodes via incorporating highly conductive Sm³⁺ and Nd³⁺ double-doped ceria for reversible solid oxide cells, *ACS Appl. Mater. Inter.* 13 (2) (2021) 2496–2506.
- [56] J. Ke, J. Xiao, W. Zhu, H. Liu, R. Si, Y. Zhang, C. Yan, Dopant-induced modification of active site structure and surface bonding mode for high performance nanocatalysts: CO oxidation on capping-free (110)-oriented CeO₂: Ln (Ln = La-Lu) nanowires, *J. Am. Chem. Soc.* 135 (2013) 15191–15200.
- [57] J. Carey, M. Nolan, Dissociative adsorption of methane on the Cu and Zn doped (111) surface of CeO₂, *Appl. Catal. B-Environ.* 197 (2016) 324–336.
- [58] H. Wang, J. Shang, Z. Xiao, P. Aprea, S. Hao, Novel construction of carbon bonds in CeO₂@C with efficiently photocatalytic activity, *Dyes Pigments* 182 (2020) 108669.
- [59] W. Wang, Y. Chen, A. Chen, X. Ma, Composite particles with dendritic mesoporous-silica cores and nano-sized CeO₂ shells and their application to abrasives in chemical mechanical polishing, *Mater. Chem. Phys.* 240 (2020) 122279.
- [60] A. Chen, X. Ma, W. Cai, Y. Chen, Polystyrene-supported dendritic mesoporous silica hybrid core/shell particles: controlled synthesis and their pore size-dependent polishing behavior, *J. Mater. Sci.* 55 (2020) 577–590.
- [61] A. Chen, J. Qin, Z. Li, Y. Chen, Engineering functionalized PS/mSiO₂ composite particles with controlled meso-shell thickness for chemical mechanical planarization applications, *J. Mater. Sci.: Mater. Electron.* 28 (1) (2017) 284–288.
- [62] Y. Chen, Z. Li, J. Qin, A. Chen, Monodispersed mesoporous silica (mSiO₂) spheres as abrasives for improved chemical mechanical planarization performance, *J. Mater. Sci.* 51 (12) (2016) 5811–5822.
- [63] J. Ryu, W. Kim, J. Yun, K. Lee, J. Lee, H. Yu, J.H. Kim, J.J. Kim, J. Jang, Fabrication of uniform wrinkled silica nanoparticles and their application to abrasives in chemical mechanical planarization, *ACS Appl. Mater. Interfaces* 10 (14) (2018) 11843–11851.
- [64] P. Gao, T. Liu, Z. Zhang, F. Meng, R.-P. Ye, J. Liu, Non-spherical abrasives with ordered mesoporous structures for chemical mechanical polishing介孔结构非球形磨粒的制备及其在化学机械抛光中的应用研究, *Sci. China Mater.* 64 (11) (2021) 2747–2763.
- [65] A. Chen, S. Wang, W. Cai, Z. Mu, Y. Chen, Tunable synthesis, characterization, and CMP performance of dendritic mesoporous silica nanospheres as functionalized abrasives, *Colloid Surface A* 638 (2022) 128322.
- [66] Y. Chen, W. Mu, J. Lu, Young's modulus of PS/CeO₂ composite with core/shell structure microspheres measured using atomic force microscopy, *J. Nanopart. Res.* 17 (2012) 696.
- [67] A. Chen, C. Qian, Y. Chen, X. Zhao, N. Miao, Exploring the elastic behavior of core-shell organic-inorganic spherical particles by AFM indentation experiments, *J. Inorg. Organomet. Polym.* 24 (6) (2014) 1070–1076.
- [68] A. Chen, W. Mu, Y. Chen, Compressive elastic moduli and polishing performance of non-rigid core/shell structured PS/SiO₂ composite abrasives evaluated by AFM, *Appl. Surf. Sci.* 290 (2014) 433–439.
- [69] Y. Chen, C. Qian, N. Miao, Atomic force microscopy indentation to determine mechanical property for polystyrene-silica core-shell hybrid particles with controlled shell thickness, *Thin Solid Films* 579 (2015) 57–63.
- [70] X.U. Cao, G. Pan, P. Huang, D. Guo, G. Xie, Silica-coated core-shell structured polystyrene nanospheres and their size-dependent mechanical properties, *Langmuir* 33 (33) (2017) 8225–8232.
- [71] H. Akbari Moayeri, M. Naderi, J. Aghazadeh Mohandes, Synthesis and nanomechanical properties of polystyrene/silica core/shell particles via atomic force microscopy, *Langmuir* 37 (35) (2021) 10602–10611.
- [72] S. Ozden, C.S. Tiwary, J.Y. Yao, G. Brunetto, S. Bhowmick, S. Asif, R. Vajtai, P. M. Ajayan, Highly ordered carbon-based nanospheres with high stiffness, *Carbon* 105 (2016) 144–150.
- [73] E. Wachtel, I. Lubomirsky, The elastic modulus of pure and doped ceria, *Scripta Mater.* 65 (2) (2011) 112–117.
- [74] N. Yavo, D. Noiman, E. Wachtel, S. Kim, Y. Feldman, I. Lubomirsky, O. Yeheskel, Elastic moduli of pure and gadolinium doped ceria revisited: Sound velocity measurements, *Scripta Mater.* 123 (2016) 86–89.
- [75] X. Chen, Y. Zhao, Y. Wang, Modeling the effects of particle deformation in chemical mechanical polishing, *Appl. Surf. Sci.* 258 (22) (2012) 8469–8474.
- [76] L. Wang, P. Zhou, Y. Yan, B. Zhang, R. Kang, D. Guo, Chemical-mechanical wear of monocrystalline silicon by a single pad asperity, *Int. J. Mach. Tool Manu.* 120 (2017) 61–71.
- [77] C. Qin, Z. Hu, A. Tang, Z. Yang, S. Luo, An efficient material removal rate prediction model for cemented carbide inserts chemical mechanical polishing, *Wear* 452–453 (2020) 203293.
- [78] Y. Wang, Y. Chen, F. Qi, D. Zhao, W. Liu, A material removal model for silicon oxide layers in chemical mechanical planarization considering the promoted chemical reaction by the down pressure, *Tribol. Int.* 93 (2016) 11–16.
- [79] L.M. Cook, Chemical processes in glass polishing, *J. Non-Cryst. Solid* 120 (1-3) (1990) 152–171.
- [80] T. Hoshino, Y. Kurata, Y. Terasaki, K. Susa, Mechanism of polishing of SiO₂ films by CeO₂ particles, *J. Non-Cryst. Solids* 283 (2001) 129–136.
- [81] T. Onodera, H. Takahashi, S. Nomura, First-principles molecular dynamics investigation of ceria/silica sliding interface toward functional materials design for chemical mechanical polishing process, *Appl. Surf. Sci.* 530 (2020) 147259.
- [82] K.K. Myong, J. Byun, M. Choo, H. Kim, J.Y. Kim, T. Lim, J.J. Kim, Direct and quantitative study of ceria-SiO₂ interaction depending on Ce³⁺ concentration for chemical mechanical planarization (CMP) cleaning, *Mat. Sci. Semicon. Proc.* 122 (2021) 105500.
- [83] C.A. Nieves, A. Meléndez, N.J. Pinto, I. Ramos, Facile fabrication of carbon spheres/n-Si junction diodes based on sucrose, *J. Mater. Sci.: Mater. Electron.* 27 (12) (2016) 13044–13051.
- [84] S. Akshatha, L. Parashuram, V.U. Kumar, F.A. Alharthi, T.M.C. Rao, S. Kumar, Microwave assisted green synthesis of p-type Co₃O₄@Mesoporous carbon spheres for simultaneous degradation of dyes and photocatalytic hydrogen evolution reaction, *Mat. Sci. Semicon. Proc.* 121 (2021) 105432.
- [85] M.A. Mavuso, P.R. Makgware, S.S. Ray, Heterostructured CeO₂-M (M = Co, Cu, Mn, Fe, Ni) oxide nanocatalysts for the visible-light photooxidation of pinene to aromatic oxygenates, *ACS Omega* 5 (17) (2020) 9775–9788.
- [86] Y. Lin, Z. Wu, J. Wen, K.R. Poepelmeier, L.D. Marks, Imaging the atomic surface structures of CeO₂ nanoparticles, *Nano Lett.* 14 (1) (2014) 191–196.
- [87] B. Goris, S. Turner, S. Bals, G. Van Tendeloo, Three-dimensional valency mapping in ceria nanocrystals, *ACS Nano* 8 (10) (2014) 10878–10884.
- [88] Y.Z. Hu, R.J. Gutmann, T.P. Chow, Silicon nitride chemical mechanical polishing mechanisms, *J. Electrochem. Soc.* 145 (11) (1998) 3919–3925.
- [89] S.R. Gilliss, J. Bentley, C.B. Carter, Nanochemistry of ceria abrasive particles, *Mater. Res. Soc.* 818 (2004) 9–14.

- [90] W.G. America, S.V. Babu, Slurry additive effects on the suppression of silicon nitride removal during CMP, *Electrochim. Solid-State Lett.* 7 (2004) G327–G330.
- [91] T. Pirmohamed, J.M. Dowding, S. Singh, B. Wasserman, E. Heckert, A.S. Karakoti, J.E. King, S. Seal, W.T. Self, Chem. Nanoceria exhibit redox state-dependent catalase mimetic activity, *Chem. Commun.* 46 (2010) 2736–2738.
- [92] N. Ozawa, M. Ishikawa, M. Nakamura, M. Kubo, Polishing process simulation of SiO₂ by CeO₂ abrasive grain under wet environment, *Hyomen, Kagaku* 33 (6) (2012) 351–356.
- [93] C.M. Netzband, K. Dunn, Controlling the cerium oxidation state during silicon oxide CMP to improve material removal rate and roughness, *ECS J. Solid State Sci. Technol.* 9 (2020), 044001.